



Improving leaf area index retrieval over heterogeneous surface mixed with water



Baodong Xu^{a,b,c}, Jing Li^{a,*}, Taejin Park^b, Qinhua Liu^{a,*}, Yelu Zeng^d, Gaofei Yin^e, Kai Yan^f, Chi Chen^b, Jing Zhao^a, Weiliang Fan^g, Yuri Knyazikhin^b, Ranga B. Myneni^b

^a State Key Laboratory of Remote Sensing Science, Jointly Sponsored by Aerospace Information Research Institute, Chinese Academy of Sciences and Beijing Normal University, Beijing 100101, China

^b Department of Earth and Environment, Boston University, Boston, MA 02215, USA

^c Macro Agriculture Research Institute, College of Resource and Environment, Huazhong Agricultural University, Wuhan 430070, China

^d Department of Global Ecology, Carnegie Institution for Science, Stanford, CA 94305, USA

^e Faculty of Geosciences and Environmental Engineering, Southwest Jiaotong University, Chengdu 610031, China

^f School of Land Science and Techniques, China University of Geosciences, Beijing 100083, China

^g School of Environmental and Resources Science, Zhejiang A & F University, Lin'an 311300, China

ARTICLE INFO

Edited by: Jing M. Chen

Keywords:

Subpixel mixture
Leaf area index (LAI)
Water effects
Uncertainty
MODIS collection 6

ABSTRACT

Land cover mixture at moderate- to coarse-resolution is an important cause for the uncertainty of global leaf area index (LAI) products. The accuracy of LAI retrievals over land-water mixed pixels is adversely impacted because water absorbs considerable solar radiation and thus can greatly lower pixel-level reflectance especially in the near-infrared wavelength. Here we proposed an approach named Reduced Water Effect (RWE) to improve the accuracy of LAI retrievals by accounting for water-induced negative bias in reflectances. The RWE consists of three parts: water area fraction (WAF) calculation, subpixel water reflectance computation in land-water mixed pixels and LAI retrieval using the operational MODIS LAI algorithm. The performance of RWE was carefully evaluated using the aggregated Landsat ETM+ reflectance of water pixels over different regions and observation dates and the aggregated 30-m LAI reference maps over three sites in the moderate-resolution pixel grid (500-m). Our results suggest that the mean absolute errors of water endmember reflectance in red and NIR bands were both < 0.016, which only introduced mean absolute (relative) errors of < 0.15 (15%) for the pixel-level LAI retrievals. The validation results reveal that the accuracy of RWE LAI was higher than that of MODIS LAI over land-water mixed pixels especially for pixels with larger WAFs. Additionally, the mean relative difference between RWE LAI and aggregated 30-m LAI did not vary with WAF, indicating that water effects were significantly reduced by the RWE method. A comparison between RWE and MODIS LAI shows that the maximum absolute and relative differences caused by water effects were 0.9 and 100%, respectively. Furthermore, the impact of water mixed in pixels can induce the LAI underestimation and change the day selected for compositing the 8-day LAI product. These results indicate that RWE can effectively reduce water effects on the LAI retrieval of land-water mixed pixels, which is promising for the improvement of global LAI products.

1. Introduction

The importance of vegetation is well recognized in studies of land-atmosphere interactions (Sellers et al., 1997; Simonich and Hites, 1994). Leaf area index (LAI), which is defined as one half of the total green leaf area per unit ground surface area (Chen and Black, 1992; Jonckheere et al., 2004), is extensively used to characterize the structure and function of vegetation (Garrigues et al., 2008). As the leaf is the primary interface for the exchange of energy and mass between the

canopy and atmosphere, LAI is a critical parameter in terrestrial ecosystem models and plays an important role in the simulation of land surface processes, such as photosynthesis, respiration and transpiration (Bonan, 1995; Liu et al., 1997). Therefore, obtaining highly accurate LAI datasets is very important for their proper use in land surface models and various user communities (Bi et al., 2015; Yin et al., 2017; Zhu et al., 2016).

To acquire long-term LAI time series at the global scale, several remote sensing LAI products have been generated from various satellite

* Corresponding authors.

E-mail addresses: lijing01@radi.ac.cn (J. Li), liuqh@radi.ac.cn (Q. Liu).

sensors, such as MODIS, VEGETATION and AVHRR (Baret et al., 2007; Baret et al., 2013; Ganguly et al., 2008; Myneni et al., 2002; Xiao et al., 2016). A number of previous studies have evaluated uncertainties associated with different LAI products through comparisons with independent ground-truth measurements (i.e., direct validation) at regional to global levels on different observation dates (Camacho et al., 2013; Fang et al., 2012; Garrigues et al., 2008; Weiss et al., 2007; Xiao et al., 2017). However, the integrated validation results at the spatio-temporal scale show that the uncertainty of LAI products cannot meet the uncertainty requirement (max (0.5, 20%)) suggested by the Global Climate Observing System (GCOS) (GCOS, 2011). Three key factors, i.e., uncertainties from input land cover maps, surface reflectances, and the retrieval algorithm, were identified to influence the accuracy of LAI retrievals (Yang et al., 2006), and these factors are closely related to the heterogeneity of land surface. Specifically, the most important characteristic of heterogeneous surfaces is the mixture of different land cover types (Yin et al., 2015). To date, global LAI products are available at 500-m, 1-km or even coarser spatial resolutions, which inevitably suffer from the effect of land cover mixtures. Based on a 30-m global land cover dataset (Chen et al., 2014), the proportion of mixed pixels in the 1-km pixel grid is > 65% of the global land area (Yu et al., 2018). Unfortunately, current LAI retrieval algorithms assume that each pixel is only occupied by one land cover type, which introduces errors for moderate- or coarse-resolution LAI estimations due to land cover mixtures within a pixel grid (Chen et al., 2002; Garrigues et al., 2006).

The impact of land cover mixtures at the subpixel scale on LAI estimations is of great interest and has drawn the attention of various studies. A sensitivity analysis indicated that the vegetation fraction in a pixel is the dominant factor for determining the reflectance of this pixel at the region scale (Xiao et al., 2014a). As a result, it was ever reported that the LAI difference between mixed and pure pixels can reach 178% for savanna (Fang et al., 2013). Generally, LAI retrieval errors are inversely related to the proportion of the dominant land cover type in a coarse-resolution pixel (Tian et al., 2002), and the biases in coarse-resolution LAI maps can be removed using subpixel land cover data (Jin et al., 2007). Therefore, the accuracy of LAI retrievals can be significantly improved if the effect of subpixel mixture is considered (Wu et al., 2013; Yin et al., 2015). Despite the recognition for the importance of subpixel information, the effective methods of addressing land cover mixtures for the generation of global moderate- or coarse-resolution LAI products have not been comprehensively developed. This challenging is likely because the area proportions of different land cover types in moderate- or coarse-resolution pixels are not easy to obtain at the global scale. Recently, a global land cover dataset at 30-m resolution has been developed (Chen et al., 2014), which is promising to derive the proportions of land cover types within the coarse-resolution pixels and then to reduce the errors of subpixel land cover mixtures for LAI retrievals.

Among the various land cover mixtures, water body is one of the main land cover types in mixed pixels at the global scale (Xu et al., 2004; Yu et al., 2018). Compared to vegetation, water generally absorbs more solar radiation and has lower reflectance in both red and near-infrared (NIR) bands. Once a pixel contains water, the reflectance of this pixel will be greatly reduced. As a consequence, the estimated LAI without considering the water effect in the land-water mixed pixels can be decreased by > 70% compared to the actual LAI over conifer forests (Chen, 1999). Due to the significant decrease in LAI caused by the water mixture, many efforts have been made to reduce the water effect to improve the accuracy of LAI retrievals (Chen et al., 2002; Xu et al., 2004). However, previous studies have two limitations that need to be further addressed for the improvement of global LAI products. First, the method of reducing the water effect in the land-water mixed pixels was based on the empirical relationships between LAI and vegetation indices (Xu et al., 2004), which is not suitable for being generalized to large regions or over a long period of time because these empirical relationships are generally site- and sensor-specific (Tian et al., 2000).

In contrast, physically-based models, which simulate the relationship between LAI and other factors (such as reflectance, sun-sensor geometries, etc.) by considering the physical processes involving photon transport within the vegetation canopy, are practical for LAI estimations under various situations at the global scale (Tian et al., 2000). Second, the spatially and temporally varying water reflectances have not been considered because the water endmember reflectance was set to a constant value in previous studies (Chen, 1999; Xu et al., 2004). The constant reflectance of the water endmember in different regions or seasons may introduce undesired errors in the generation of LAI products. Therefore, these limitations highlight the need to develop an effective method for reducing the water effects in global moderate- or coarse-resolution pixels to further improve the accuracy of LAI retrievals.

The objective of this study is to develop a new method, named Reduced Water Effects (RWE), which is capable of accounting for the water-mixture impacts and improving the accuracy of LAI retrievals over land-water mixed pixels. The RWE is expected to have two major advantages over previous studies: (1) considers the spatio-temporal variation in water endmember reflectance globally and (2) is applicable for global-scale LAI retrievals because of its basis on a physically-based model. This paper is organized as follows. Section 2 presents the framework of the RWE method, including the generation of the water endmember reflectance in land-water mixed pixels and the description of LAI retrieval algorithm. Section 3 introduces the data and detailed methods in this study. In Section 4, the uncertainty of water endmember reflectance in mixed pixels and its impact on LAI retrievals were evaluated. Then the RWE was assessed to determine whether it can improve the accuracy of LAI retrievals and the water effects on the LAI retrieval algorithm as well as LAI products were deeply analyzed. The limitations and future prospects of this study were also discussed in this section. Finally, Section 5 provides concluding remarks on this study.

2. Framework of the RWE method

2.1. Theoretical background

Based on the theoretical formulation of LAI retrievals, LAI on the observation date (t) for a specific land cover type can be illustrated as a function with several variables, such as reflectance (ρ_{Red} , ρ_{NIR}), solar geometries (zenith ($SZen$) and azimuth ($SAZi$) angles), view geometries (zenith ($VZen$) and azimuth ($VAZi$) angles), etc., that are observed on the same date. The formula is shown in Eq. (1).

$$LAI(t) = f(\rho_{red}(t), \rho_{NIR}(t), SZen(t), SAZi(t), VZen(t), VAZi(t) \dots) \quad (1)$$

For a land-water mixed pixel, both land and water endmembers share the same solar and view geometries, and the water reflectance in the mixed pixel introduces large errors to the actual land reflectance. In this study, a spectral linear mixture (SLM) model was utilized to isolate the water endmember reflectance from the whole pixel as described in Eq. (2), based on which the final land endmember reflectance without the water effects can be written as Eq. (3) (Xu et al., 2004):

$$\rho = w\rho_w + (1 - w)\rho_l \quad (2)$$

$$\rho_l = \frac{\rho - w\rho_w}{1 - w} \quad (3)$$

where ρ is the whole pixel reflectance, and ρ_w and ρ_l denote the reflectance of water and land endmembers, respectively. The variable w is the water area fraction (WAF) in the coarse-resolution pixel grid which can be calculated from high-resolution land cover maps. If the water endmember reflectance can be derived in land-water mixed pixels, we can use it to extract the land endmember reflectance (Eq. (3)) and calculate the subpixel LAI (Eq. (1)) as well as the whole pixel LAI without water effects. Therefore, RWE includes three sequential

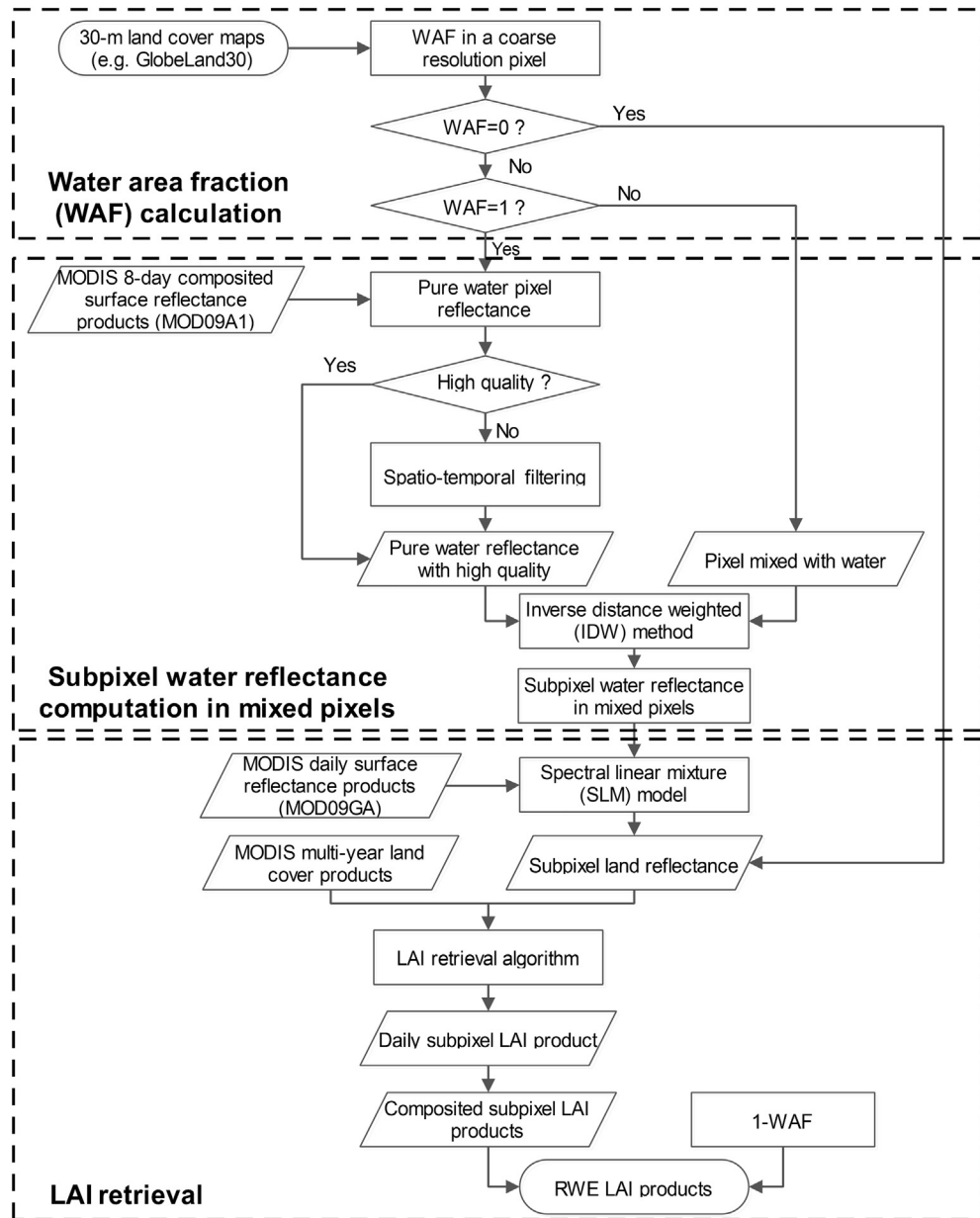


Fig. 1. The framework of the RWE method.

processes: (1) WAF calculation for all pixels, (2) subpixel water reflectance computation in land-water mixed pixels and (3) pixel-level LAI retrieval. The flowchart of the RWE method is shown in Fig. 1. First, the WAF is calculated using 30-m global land cover maps. Then, the water endmember reflectance in the land-water mixed pixel is derived using the reflectance of high-quality pure water pixels generated by a spatio-temporal filtered method (see Appendix A). Finally, the subpixel land reflectance is input into the LAI retrieval algorithm to generate the subpixel LAI, which is then combined with land area fraction to calculate the whole pixel LAI. The details of the latter two processes are provided in Sections 2.2–2.3.

2.2. Subpixel water reflectance computation in land-water mixed pixels

Due to the spatial correlation of the land surface characteristics, the water endmember reflectance in the land-water mixed pixel is strongly related to that of the adjacent pure water pixels and is calculated based on these adjacent pure water pixels in the RWE method. Thus, the reflectance of high-quality pure water pixels should be carefully selected.

First, pure water pixels ($\text{WAF} = 1$) were identified using high-resolution (e.g. 30-m) land cover maps. Then, given the spatio-temporal variation of water reflectance, the MODIS 8-day composite surface reflectance product (MOD09A1) was employed because it can provide global water reflectance every 8 days since the year 2000. Even though MODIS provides daily reflectance products (MOD09GA), MOD09A1 has better quality than MOD09GA because it selected the best observation from daily MOD09GA during an 8-day period on the basis of high observation coverage, low view angle, absence of clouds or cloud shadow, and aerosol loading (Vermote et al., 2015). In this study, we assume that the water reflectance is similar during the 8-day composited period. According to the cloud and snow/ice information provided by the MOD09A1 State quality assessment (QA) layer and the valid range (0–0.1) of water reflectances, pure water pixels with different observation qualities were categorized into three levels, i.e., Levels 0–2 (Supplementary material, Fig. S1). Level 0 indicates the best-quality reflectance of pure water pixels followed by Level 1 and Level 2. However, due to the impact of cloud, snow and other factors, the proportion of high-quality pure water pixels is generally quite low. For

example, Level 0 pixels account for only 57% of all pure water pixels in one MODIS tile (H13V04 on 19 July 2000), which is insufficient to generate the water endmember reflectance in mixed pixels. Therefore, a spatio-temporal filtering method, named the modified temporal spatial filter (mTSF) proposed by Yuan et al. (2011), was adopted to reprocess the reflectance of Levels 1–2 pure water pixels to obtain more high-quality reflectances (see Appendix A for details).

Since the water reflectance of a pixel is often similar to those of neighboring pixels and is different with those farther away (Supplementary material, Fig. S2), we utilized the inverse distance weighted (IDW) method to interpolate the water endmember reflectance in mixed pixels based on all spatio-temporally filtered reflectances of pure water pixels. Specifically, the window size (3×3 , $5 \times 5\ldots$) was centered over each land-water mixed pixel to search for the adjacent pure water pixels. In this study, the number of nearest pure water pixels was set to 100 because this empirically driven number is expected to reduce the uncertainty of potentially abnormal pixels and also guarantee the representatives of water reflectance in spatial distance. If > 100 pure water pixels were found for the land-water mixed pixel, the water endmember reflectance in the mixed pixel would be calculated using Eq. (4):

$$\rho_m = \sum_{i=1}^n \frac{\sqrt{(x_m - x_i)^2 + (y_m - y_i)^2}}{\sum_{i=1}^n \sqrt{(x_m - x_i)^2 + (y_m - y_i)^2}} \rho_{ip} \quad (n \geq 100) \quad (4)$$

where ρ_m and ρ_{ip} represent the water reflectance for the m th land-water mixed pixel and i th pure water pixel, respectively. x_m and y_m are the row and column numbers of the land-water mixed pixel, while x_i and y_i are the row and column numbers of the pure water pixel, respectively.

2.3. LAI retrieval algorithm

The algorithm for the latest MODIS LAI product (Collection 6, C6) was adopted in this study. The widely used MODIS C6 LAI products were generated at 500-m spatial resolution with an 8-day interval since 2000 using the main or back-up algorithm. The main algorithm is based on the biome-specific look-up tables (LUTs) simulated from the three-dimensional (3D) radiative transfer (RT) model (Knyazikhin et al., 1998; Shabanov et al., 2005). With the inputs of the daily MODIS red and NIR atmospherically corrected reflectances and the corresponding sun-view geometries, the mean LAI is calculated from all the LAI elements for which the corresponding simulated reflectances in the LUTs are close to the MODIS reflectances within specific uncertainties. When the main algorithm fails caused by cloud effects or too low sun/view zenith angles, the back-up algorithm based on the LAI-NDVI relationships for each biome is used to retrieve LAI (Myneni et al., 2002). Finally, the LAI corresponding to the maximum Fraction of Photosynthetically Active Radiation absorbed by vegetation (FPAR) over an 8-day period is selected as the composited product value.

It is essential to improve the accuracy of LAI retrievals based on the latest MODIS LAI products for two reasons. On one hand, the MODIS LAI product is noteworthy because it is developed using a physically-based radiative transfer algorithm, and is therefore suitable for global LAI retrievals. On the other hand, the MODIS LAI product has been employed as the benchmark to generate other global LAI products, such as GLASS (Xiao et al., 2014b) and GEOV1 (Baret et al., 2013). The LAI retrieval process of land-water mixed pixels is illustrated in the “LAI retrieval” part of Fig. 1. First, the subpixel water reflectances at both red and NIR bands were removed from the daily reflectance products based on the SLM model. Then, the subpixel land reflectance and land cover map were combined to retrieve the daily LAI as well as the 8-day composited LAI using the MODIS LAI retrieval algorithm. Finally, the pixel-level LAI products were calculated by multiplying the subpixel LAI and the associated land area fraction. Therefore, the difference between the MODIS and RWE LAI retrievals for land-water mixed pixels

is that MODIS LAI products were generated using the reflectance of the whole pixel, whereas RWE LAI retrievals were derived using the sub-pixel land reflectance as well as the land area fraction in the coarse-resolution pixel grid (Supplementary material, Fig. S3).

3. Data and methods

3.1. 30-m global land cover maps

The global land cover maps at 30-m spatial resolution (GlobeLand30, <http://www.globallandcover.com>), produced by National Geomatics Center of China (Chen et al., 2014) for the year 2000 and 2010, were used to calculate the WAF in the land-water mixed pixels and identify the pure water pixels at the global scale in this study. The primary data sources for generating GlobeLand30 of 2000 and 2010 were Landsat TM/ETM+ images worldwide, with an additional use of Chinese Environmental and Disaster satellite (HJ-1) images for the year 2010 (Chen et al., 2015). The classification approach was based on the integration of pixel- and object-based methods with knowledge (POK-based), and then a knowledge-based interactive verification procedure was developed to improve the classification quality (Chen et al., 2015). GlobeLand30 includes 10 land cover types, among which water bodies have the classification accuracy of approximately 90% for both 2000 and 2010 according to previous studies (Bratic et al., 2018; Brovelli et al., 2015; Manakos et al., 2015). The reported accuracy imbues our confidence in the classification of water bodies and suggests a good reliability of the WAF calculation.

3.2. Study area and high-resolution LAI reference maps

To evaluate the performance of LAI retrievals using the RWE method, we selected the study area based on two criteria: (1) availability of high-resolution LAI reference maps that were generated using ground measurements; (2) the existence of water bodies in this region. For this purpose, four MODIS tiles (H13V04, H12V03 and H11V02-H11V03) located in Canada were selected based on global-scale or continental-scale ground-observing programs, as shown in Fig. 2a–c. These tiles cover three sites, i.e., Kejimikujik, Thompson and Watson Lake, for which ground-based 30-m LAI reference maps were generated using Landsat images on 15 July 2000, 15 July 2001 and 15 July 2000, respectively (Fernandes et al., 2005). The Kejimikujik site (red polygon in Fig. 2a) is located in southern Canada and fall within the temperate continental forest system according to the FAO global ecological zones (<http://www.fao.org/geonetwork>, July 2019). According to the MODIS land cover dataset (MCD12Q1), the biome types of this site are needleleaf forest and broadleaf forest, accounting for 66.7% and 32.8% of the total land area, respectively. The Thompson and Watson Lake sites (red polygons in Fig. 2b–c) are located in western and southern Canada and their ecosystems are boreal coniferous forest and boreal mountain system, respectively. The dominant land cover in these two sites is needleleaf forest (40.0% for the Thompson site and 58.9% for the Watson Lake site). The valid area of the 30-m LAI reference map (Fig. 2d–f) is approximately 900 km², 20,300 km² and 16,000 km² for the three sites, respectively, which accounts for 0.06%, 1.41% and 0.56% in each study area. Based on the accuracy report from Fernandes et al. (2005), the median absolute errors of ground-based LAI reference maps were respectively 0.42, 0.33 and 0.36 for the three sites. Due to the reasonable accuracy of the LAI reference maps (Camacho et al., 2013) and the inclusion of land-water mixed pixels in the corresponding region, these ground-based LAI reference maps can be utilized to evaluate the performances of MODIS and RWE LAI retrievals in the 500-m pixel grid. It is noteworthy that the LAI values provided by reference maps are the true LAI because the clumping effect was considered in the field measurements (Fernandes et al., 2005).

Additionally, all pixels except ocean pixels in four tiles were counted as valid pixels, and the associated number and proportion in

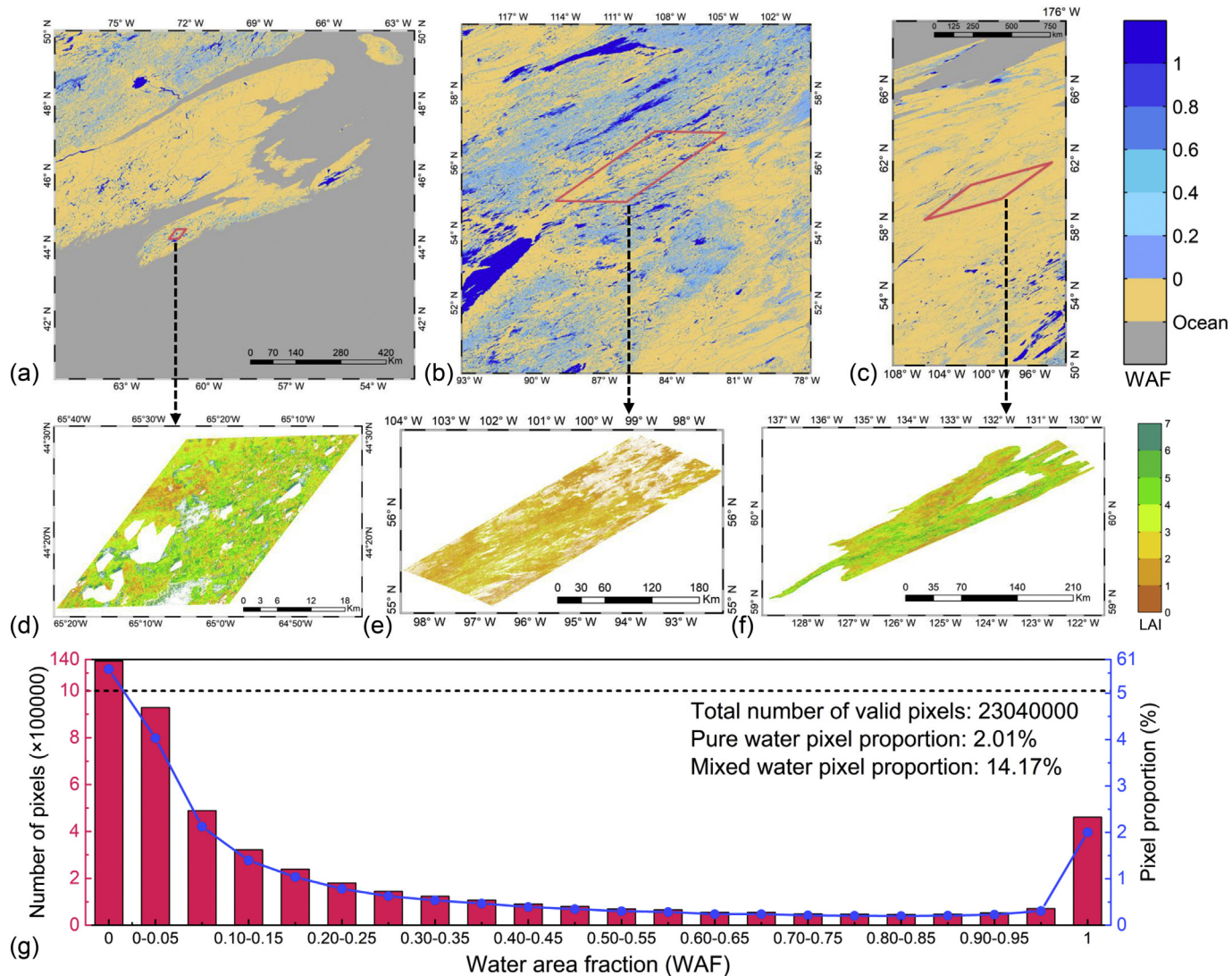


Fig. 2. The spatial distributions of the WAFs in the (a) H13V04, (b) H12V03 and (c) H11V02-H11V03 tiles. An equal-area sinusoidal projection is used here. The gray and yellow colors denote ocean and no subpixel water in the pixel grid, respectively. The red polygon in each tile indicates the extent of the available ground-based high-resolution (30-m) LAI reference map. (d–f) show the details in 30-m LAI reference maps for the Kejimikujik site on 15 July 2000, the Thompson site on 15 July 2001 and the Watson Lake site on 15 July 2000, respectively. (g) The histogram of the number (red bars) and proportion (blue line) of pixels in the different WAFs for the four tiles. (For interpretation of the references to color in this figure legend, the reader is referred to the web version of this article.)

different WAFs are shown in Fig. 2g. These study areas have over 23 million 500-m valid pixels, and the proportions of pure water and land-water mixed pixels are 2.01% and 14.17%, respectively. As expected, both the number and proportion of land-water mixed pixels decreased as the WAF increased. Due to the limited spatial coverage of ground-based LAI reference maps, these four tiles were used to evaluate the water effects on LAI retrievals over a large number of pixels based on the intercomparison between MODIS LAI products and RWE LAI retrievals.

3.3. Landsat TM/ETM+ reflectance

Given the high spatial resolution allows us to obtain the reflectance of pure water pixels (e.g., 30-m) in the 500-m pixel grid, the 30-m Landsat TM/ETM+ surface reflectance data, which were downloaded from the USGS Earth Resources Observation and Science (EROS) Center Science Processing Architecture (ESPA) On Demand Interface (<https://espa.cr.usgs.gov/>), were used to evaluate the performance of the generated water endmember reflectance in the land-water mixed pixels. The Landsat Ecosystem Disturbance Adaptive Processing System

(LEDAPS) software applies MODIS atmospheric correction routines to Level-1 Landsat TM/ETM+ data, which inputs water vapor, ozone, geopotential height, aerosol optical thickness, and digital elevation to Second Simulation of a Satellite Signal in the Solar Spectrum (6S) radiative transfer models to generate the surface reflectance (Masek et al., 2006). The Landsat surface reflectance products also provide a quality description layer (pixel_qa) to identify clouds, cloud shadows, snow, or water for each pixel. In order to comprehensively evaluate the performance of the derived water endmember reflectance over different regions and observation dates, a total of 20 Landsat ETM+ surface reflectance scenes in two MODIS tiles were carefully selected from all available ETM+ data during year 2000–2002, as shown in Table 1. It is noteworthy that these selected scenes were less contaminated by clouds or snow/ice according to the quality description layer and their observation dates were close to that of MODIS tiles.

Furthermore, only reflectances of clear water pixels extracted from Landsat ETM+ were used to evaluate the accuracy of the water endmember reflectances in the land-water mixed pixels. Nevertheless, due to the differences in the spectral response functions (SRFs) in the red and NIR bands between Landsat (red: 0.63–0.69 μm; NIR:

Table 1

Landsat ETM + scenes and MODIS tiles over different regions and observation dates used for evaluating the uncertainty of derived water endmember reflectance in the land-water mixed pixels.

	Landsat ETM +	MODIS (MOD09A1)	Landsat ETM +	MODIS (MOD09A1)
	Path: 009 Row: 029	H: 13 V: 04	Path: 033 Row: 021	H: 12 V: 03
Observation dates (month/day/year)	06/18/2000 07/20/2000 09/06/2000 10/24/2000 08/08/2001 09/09/2001 05/07/2002 05/23/2002 06/08/2002 08/11/2002 08/27/2002	06/17/2000 07/19/2000 09/05/2000 10/23/2000 08/05/2001 09/06/2001 05/01/2002 05/17/2002 06/02/2002 08/05/2002 08/21/2002	05/25/2000 06/10/2000 07/28/2000 05/12/2001 05/28/2001 07/31/2001 09/17/2001 08/19/2002 10/06/2002	05/24/2000 06/09/2000 07/27/2000 05/09/2001 05/25/2001 07/28/2001 09/14/2001 08/13/2002 09/30/2002

0.77–0.90 μm) and MODIS (red: 0.62–0.67 μm; NIR: 0.84–0.88 μm), the Landsat reflectance cannot be directly compared with that of MODIS. Therefore, the empirical formulation provided by Liang et al. (2002) was employed to predict the reflectance in the MODIS bands from ETM + reflectance. Specifically, the predicted equations for the red and NIR bands are shown in Eqs. (5)–(6), respectively:

$$Red_{MOD} = 0.0798B2_{ETM+} + 0.9209B3_{ETM+} \quad (5)$$

$$NIR_{MOD} = 0.1711B1_{ETM+} - 0.2007B2_{ETM+} + 1.0107B4_{ETM+} + 0.0427B5_{ETM+} \quad (6)$$

where $B1_{ETM+}$ – $B5_{ETM+}$ denotes the ETM + reflectance from band 1 to band 5. Based on the evaluation results of Liang et al. (2002), the average residual errors of the predicted MODIS reflectance were < 0.01 based on hundreds of surface reflectance spectra around the year 2000. The difference of water reflectance between Landsat and MODIS caused by their view geometries was not considered in this study, which may introduce additional source of uncertainty for evaluating the MODIS-based water reflectance.

3.4. Performance evaluation of the RWE method

The proposed RWE method includes two critical processes, i.e., the generation of subpixel water reflectance and LAI inversion using MODIS LAI retrieval algorithm, which was implemented to the four MODIS tiles covering the three sites. To evaluate the performance of the RWE method, the derived subpixel water reflectance and LAI retrievals were then assessed from different perspectives described in the following subsections.

3.4.1. Evaluation of water endmember reflectance in land-water mixed pixels

The accuracy of the derived water endmember reflectance in land-water mixed pixels should be prior identified because the water endmember reflectance is an important input to calculate the subpixel land reflectance. The benchmark subpixel water reflectance within the MODIS pixel grid, which was aggregated from the Landsat ETM + image, was used to assess the water endmember reflectance in the land-water mixed pixels. The statistical metrics, including mean error (ME_ρ) and mean absolute error (MAE_ρ) of reflectance, were calculated according to Eqs. (7)–(8):

$$ME_\rho = \frac{1}{N} \sum_{i=1}^N (\rho_{iMOD} - \rho_{iETM+}) \quad (7)$$

$$MAE_\rho = \frac{1}{N} \sum_{i=1}^N |\rho_{iMOD} - \rho_{iETM+}| \quad (8)$$

where N is the total number of pixels, and ρ_{iMOD} is the derived reflectance of the water endmember in the land-water mixed pixels using the RWE method or the reflectance of MODIS pure water pixels. ρ_{iETM+} denotes the average reflectance of pure water pixels from the Landsat ETM + image in the MODIS pixel grid.

Furthermore, the impact caused by the uncertainty of water endmember reflectance on LAI retrievals for land-water mixed pixels, which was characterized by mean absolute errors (MAE_{LAI}) and mean absolute relative errors ($MARE_{LAI}$) of LAI retrievals, was investigated based on the simulated LAI retrievals in different water reflectances at red and NIR bands. Note that we set different WAFs which ranged from 0 to 0.6 with an interval of 0.1. For each WAF, the simulated LAI retrievals changed with the water endmember reflectances. The detailed calculation of MAE_{LAI} and $MARE_{LAI}$ are shown in Eqs. (9)–(10):

$$MAE_{LAI}(\Delta\rho_{red}, \Delta\rho_{NIR}) = \sum_{WAF} \sum_{\rho_{red}} \sum_{\rho_{NIR}} \frac{|LAI(\rho_{red}, \rho_{NIR}, WAF) - LAI(\rho_{red} \pm \Delta\rho_{red}, \rho_{NIR} \pm \Delta\rho_{NIR}, WAF)|}{N_{WAF} \times N_{\rho_{red}} \times N_{\rho_{NIR}}} \quad (9)$$

$$MARE_{LAI}(\Delta\rho_{red}, \Delta\rho_{NIR}) = \sum_{WAF} \sum_{\rho_{red}} \sum_{\rho_{NIR}} \frac{|LAI(\rho_{red}, \rho_{NIR}, WAF) - LAI(\rho_{red} \pm \Delta\rho_{red}, \rho_{NIR} \pm \Delta\rho_{NIR}, WAF)|}{N_{WAF} \times N_{\rho_{red}} \times N_{\rho_{NIR}} \times LAI(\rho_{red}, \rho_{NIR}, WAF)} \times 100 \quad (10)$$

($\Delta\rho_{red}/\Delta\rho_{NIR}/\rho_{red}/\rho_{NIR} = 0, 0.005, 0.01...0.095, 0.1$; $WAF = 0, 0.1...0.5, 0.6$), where $\Delta\rho_{red}/\Delta\rho_{NIR}$ and ρ_{red}/ρ_{NIR} are the errors of water endmember reflectance in red/NIR band and the water endmember reflectance in red/NIR band, $LAI(\rho_{red}, \rho_{NIR}, WAF)$ and $LAI(\rho_{red} \pm \Delta\rho_{red}, \rho_{NIR} \pm \Delta\rho_{NIR}, WAF)$ denote the LAI retrievals in different water endmember reflectances at the specific WAF, $N_{WAF}/N_{\rho_{red}}/N_{\rho_{NIR}}$ is the number of cases in different water endmember reflectances and WAFs.

3.4.2. Validation of RWE LAI using the site-based LAI reference maps

The high-resolution LAI reference maps of the three sites were used as the benchmark to assess the accuracy of RWE LAI retrievals using the correlation coefficient (R^2), bias and root mean square error (RMSE). Additionally, the uncertainty requirement (max (0.5, 20%)) of LAI retrievals set by GCOS (GCOS, 2011) was also utilized as a criterion to evaluate the improvement of RWE LAI retrievals compared to the

performance of MODIS LAI products in different WAFs. To aggregate 30-m LAI reference map to MODIS pixel grid, the LAI reference map was projected to the sinusoidal projection of MODIS LAI product suggested by Morisette et al. (2006) to reduce resampling errors. According to the quality flags of the ground-based LAI reference map, several invalid pixels were likely associated with the impact of clouds. Thus the mean LAI of the projected LAI map was calculated only if the proportion of valid pixels exceeded 60% in the 500-m pixel grid. Finally, the aggregated LAI values from 30-m reference maps were compared with MODIS and RWE LAI retrievals. It is noteworthy that the quality control was performed for both MODIS and RWE LAI retrievals to exclude pixels contaminated by clouds, cloud shadow, cirrus, and snow (Xu et al., 2018).

3.4.3. Intercomparison with MODIS LAI products in different WAFs

The water effects on the MODIS daily LAI and 8-day composited LAI products generated by the LAI retrieval algorithm were first analyzed. Then, the MODIS C6 LAI product was compared to the RWE LAI retrievals to further explore the water effects on the composited LAI products in different WAFs over a large number of land-water mixed pixels. Because both the LAI retrieval algorithm and all inputs except for the reflectances in the red and NIR bands were same for these two LAI products, their LAI differences should be attributed to the water effects for those land-water mixed pixels. Since LAI retrievals from the back-up algorithm are usually influenced by the residual clouds or poor atmospheric correction (Wang et al., 2001), only LAIs from the main algorithm were used in this study. Three metrics that characterize the differences between MODIS LAI and RWE LAI based on pixel-to-pixel calculations, i.e. Bias, RMSE and rRMSE (RMSE divided by the average of LAI retrievals), were used to quantitatively evaluate the systematic error and the total error caused by water effects.

4. Results and discussion

4.1. Evaluation of water endmember reflectance in land-water mixed pixels

The water endmember reflectance in land-water mixed pixels on 19 July 2000 was compared to the cross-sensor corrected and aggregated Landsat ETM+ surface reflectance of water pixels in the 500-m pixel grid on 20 July 2000. Fig. 3 shows the spatial patterns of water reflectance in the red and NIR band. Theoretically, the red reflectance is higher than the NIR reflectance for pure water. However, we observed the opposite trend from Fig. 3 as the water reflectances of many pixels in the red band were lower than that in the NIR band, even for pure water pixels with high-quality reflectance (Fig. 3a, d). This unexpected trend can be attributed to three aspects: (1) the spectral diversity of water bodies. For instance, clear water and turbid water display relatively lower reflectance in NIR bands, while water containing algae potentially leads to higher NIR reflectance (Sun et al., 2012); (2) the atmospheric effects. The atmosphere negatively impacts the red band more than the NIR band, which is difficult to be corrected completely because the water reflectance is very low; (3) the uncertainty of the pure water pixel identified from 500-m pixel grids, which are commonly caused by the misclassification of water bodies from 30-m land cover maps and the large off-nadir view zenith angle (VZA) of MODIS observation. Specifically, the misclassification of land to water as well as the pixel increased by a factor of six from nadir to edge of scan due to the large VZA (Yan et al., 2018) may introduce higher NIR reflectance. In addition, it should be noted that the above observations of water reflectance in red and NIR bands only referred to one small region at a single observation date. In other regions or observation dates shown in Fig. 4, the water reflectance in red band is obviously greater than NIR band. Finally, both red and NIR bands generally show similar spatial patterns between Landsat and MODIS in addition to several pixels for which MODIS presents relatively higher reflectance (Fig. 3b–c, e–f). The water reflectance maps also show that the magnitudes of their

differences were < 0.01 for the majority of the pixels.

Fig. 4 further compares aggregated ETM+ and MODIS water reflectance in pure water and land-water mixed pixels (500-m pixel grid) at red band and NIR band over different regions and observation dates, respectively. Because the whole ETM+ scene was used to evaluate the performance of the generated water endmember reflectance for each observation date, a large number of pure water pixels and land-water mixed pixels can ensure the reliability of the evaluation results. We found the variation of the aggregated ETM+ water reflectance over different regions or dates was even > 0.05 , indicating the necessity to consider the spatio-temporal variation of water reflectance. The comparison of reflectances between aggregated ETM+ and MODIS in pure water pixels exhibited slight differences, with most ME_p and MAE_p of < 0.005 and 0.015, respectively. These differences may be primarily due to the uncertainty of the cross-sensor corrected water reflectance from ETM+ to MODIS, the uncertainty of atmospheric corrections for both ETM+ and MODIS reflectances, and the difference in solar-view geometries of ETM+ and MODIS (Section 3.3). Moreover, we also observed that pure water and land-water mixed pixels almost have the same trends for the overestimation or underestimation in water reflectance when compared to the corresponding aggregated ETM+ water reflectance. This can be explained by that the reflectance of the water endmember in the land-water mixed pixel was calculated based on the adjacent pure water pixels (see Section 2.2). Moreover, the distributions of reflectance between the water endmember and the aggregated ETM+ water pixels were quite similar and the ME_p and MAE_p of derived water endmember reflectance were < 0.010 and 0.016 for both red and NIR bands based on 20 ETM+ scenes, suggesting the good performance of the proposed method. It should be noted that the errors of the generated water endmember reflectance in land-water mixed pixels also come from other sources including the uncertainties of ETM+ reflectance and predicted reflectance in the MODIS bands, despite the fact that efforts were made to reduce such sources of uncertainty.

The results in Fig. 5 indicate that both MAE_{LAI} and $MARE_{LAI}$ significantly increased with the increase of errors of water endmember reflectance, especially in red band. This is because the reflectance of vegetation in red band is much lower than NIR band and the error of water endmember reflectance in red band can introduce larger uncertainty of LAI retrievals. If the water endmember reflectance in mixed pixels was not accurate, the MAE_{LAI} and $MARE_{LAI}$ could reach > 0.5 and 100%, respectively. In this study, the ME_p and MAE_p of water endmember in both red and NIR bands were < 0.016 , which suggests that the MAE_{LAI} and $MARE_{LAI}$ would be < 0.15 and 15%, respectively. Therefore, the RWE method that takes advantage of the pure water reflectance to calculate the water endmember reflectance in land-water mixed pixels is effective and can meet the accuracy requirement of LAI retrievals.

4.2. Validation of RWE LAI using the aggregated 30-m LAI reference maps

Fig. 6 shows the comparison results between aggregated 30-m LAI reference maps and LAI retrievals and variations in uncertainties of LAI retrievals in different WAFs on 11 July 2000 for the Kejimikujik and Watson Lake sites, and 11 July 2001 for the Thompson site. Note that the results were calculated only when the WAF was > 0.05 . A total of 594 pixels were evaluated using the R^2 , bias and RMSE indicators after excluding the invalid pixels from LAI retrievals and reference maps. Overall, the comparisons of MODIS LAI and RWE LAI with the LAI reference maps indicated that the R^2 increased from 0.26 to 0.52, while the bias decreased from 0.11 to 0.02 (Fig. 6a–b). The uncertainty characterized by RMSE also decreased from 1.08 to 0.70. These statistical results suggest that RWE LAI retrievals are more accurate than MODIS LAI products. Since the variations of LAI retrievals between MODIS and RWE were dependent on the range of WAFs, all pixels were further assessed in each 0.05 interval of the WAF (Fig. 6c). The

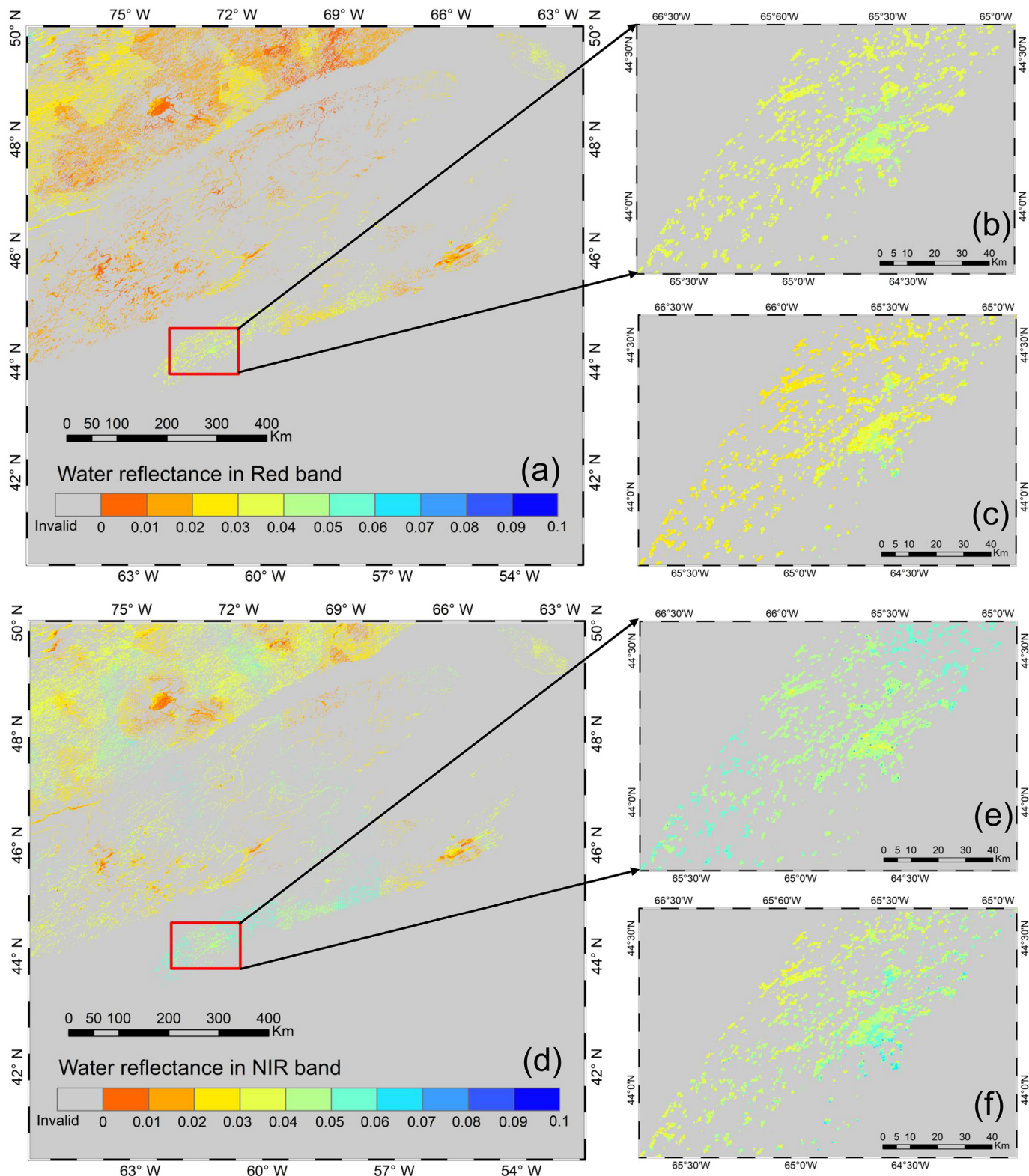


Fig. 3. The spatial patterns of water reflectance (including the reflectance of pure water pixels and water endmember in land-water pixels) in the red (a–c) and NIR (d–f) bands in the 500-m pixel grid. (a)/(d) show the reflectance in the red/NIR band for the whole MODIS tile on 19 July 2000. (b)/(e) present the selected part of the MODIS tile to compare with Landsat ETM+ water reflectance in the red/NIR band. (c)/(f) show the aggregated ETM+ water reflectance on 20 July 2000 in the 500-m pixel grid for the same region as (b)/(e) in the red/NIR band. (For interpretation of the references to color in this figure legend, the reader is referred to the web version of this article.)

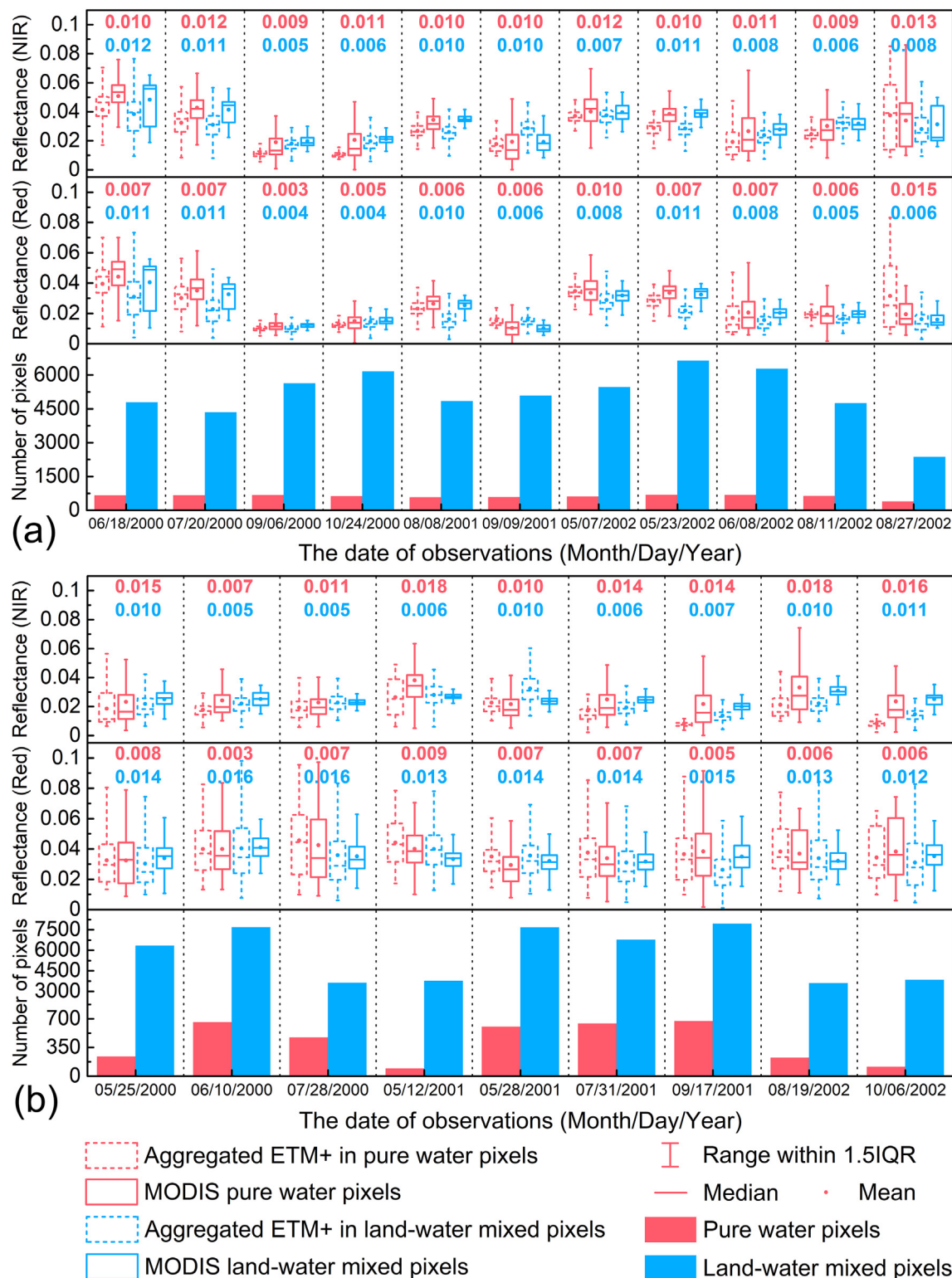


Fig. 4. A comparison between aggregated ETM+ and MODIS water reflectance in pure water and land-water mixed pixels (500-m pixel grid) at red band and NIR band. The box stretches from the 25th percentile to 75th percentile of all reflectances, while the bars indicate the range within 1.5IQR (interquartile range). The median and mean values are shown as the line and dot, respectively. (a) and (b) shows the comparison result in two regions over different observation dates during 2000–2002, and the number of valid pure water and land-water mixed pixels was also exhibited at the bottom of each figure. The red and blue numbers in each panel denote the MAE_ps for pure water and land-water mixed pixels, respectively. (For interpretation of the references to color in this figure legend, the reader is referred to the web version of this article.)

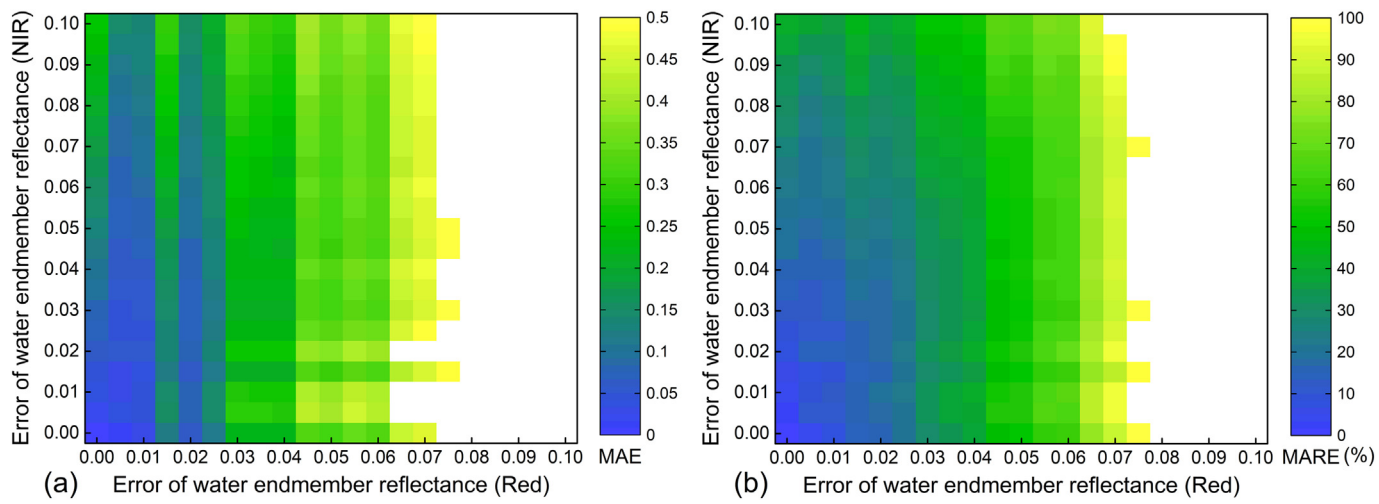


Fig. 5. The relationship between (a) mean absolute error (MAE) and (b) mean absolute relative error (MARE) of LAI retrievals and errors of water endmember reflectance in red band and NIR band. The errors of LAI retrievals were calculated from the averaged differences of LAI retrievals from various WAFs (0–0.6). The white area in (a) and (b) denotes that the MAE and MARE were > 0.5 and 100%, respectively. This figure was generated based on the LAI simulation for the deciduous broadleaf forest, with solar zenith angle of 30°, solar azimuth angle of 60°, view zenith angle of 0°, and view azimuth angle of 120°. The pixel reflectances in the red and NIR bands were 0.06 and 0.14, respectively. The derived LAI without water impacts using these solar-view geometries and reflectances at red and NIR bands was 0.6. The reflectances of water endmember in both the red and NIR bands were between 0.005 and 0.1, with the sampling interval was 0.005. (For interpretation of the references to color in this figure legend, the reader is referred to the web version of this article.)

validation results were quantitatively analyzed based on RMSE (upper panel) and the proportion of pixels (lower panel) that met the uncertainty requirement suggested by GCOS (< max (0.5, 20%)). Overall, when the WAF in the pixel was small (< 0.1), the variation of RMSE and the proportion between MODIS and RWE LAI were < 0.3 and 15%, respectively, whereas when the WAF was large, both the RMSE and the proportion substantially changed. For example, when the WAF ranged from 0.4 to 0.45, the RMSE decreased from 1.39 to 0.54, while the proportion of pixels increased from 20.1% to 66.7%. Therefore, the accuracy of the LAI retrievals can be significantly improved after reducing water effects for the land-water mixed pixels.

Additionally, the differences (mean Δ LAI and mean relative Δ LAI, Δ LAI = $|LAI_{\text{retrievals}} - LAI_{\text{reference}}|$) and relative Δ LAI = $100 \times |LAI_{\text{retrievals}} - LAI_{\text{reference}}| / LAI_{\text{reference}}$ between the MODIS or RWE LAI retrievals and the aggregated LAI reference maps were also calculated in different WAFs (Fig. 6d). Due to the influence of water mixture, the mean Δ LAI of the MODIS LAI increased when the WAF was large. In contrast, the mean Δ LAI of the RWE LAI decreased with the increase in WAFs. This trend occurred as expected because a high WAF is necessarily associated with a low LAI due to the trade-off between water area and land area within a pixel. With regard to the mean relative Δ LAI, it prominently increased for MODIS LAI with the increase in WAF and the maximum could reach 82%. However, the trend of the mean relative Δ LAI for RWE LAI was almost stable (approximately 30%) across different WAFs. These results indicate that the accuracies of RWE LAI were no longer susceptible to the change in WAF after reducing water effects, which also demonstrates the good performance of the RWE method for the LAI retrieval of land-water mixed pixels. However, more land-water mixed pixels should be obtained in different locations on different dates to achieve a more comprehensive evaluation result. Therefore, we performed additional analyses to understand the water effects on the LAI retrieval algorithm through the comparison between RWE and MODIS LAI over a large number of land-water mixed pixels.

4.3. Analysis of water effects on the LAI retrieval algorithm

Fig. 7 shows the variation in LAI and LAI relative error (RE) with the bidirectional reflectance factors (BRFs) at the red and NIR bands, which can be utilized to illustrate the water effects in the LAI retrieval

algorithm. First, because the water BRFs are generally less than the vegetation BRFs in both red and NIR bands, the pixel BRFs will increase when the water BRFs are removed. In the LAI retrieval algorithm, the potential movement of the pixel BRFs in red-NIR spectral space after removing the subpixel water reflectance can be divided into 3 cases: (1) $\Delta BRF_{\text{red}} < \Delta BRF_{\text{NIR}}$; (2) $\Delta BRF_{\text{red}} = \Delta BRF_{\text{NIR}}$; (3) $\Delta BRF_{\text{red}} > \Delta BRF_{\text{NIR}}$, as shown in Fig. 7a. Due to the larger BRF in the NIR band than the red band, the first case represents the main change in the pixel BRFs. Therefore, if a pixel is mixed with water, the pixel LAI will change obviously because of the water effects. Fig. 7b shows the LAI RE changes in different BRFs of vegetation area at red and NIR bands. When the LAI magnitude was low (LAI < 1 in Fig. 7a), the LAI RE can reach 100%, indicating that LAI was significantly overestimated for the mixed pixel. Note that this large overestimation was also caused by the low LAI (< 1 in Fig. 7a) because the small change in LAI can result in abnormally large variation of RE. However, when the LAI of vegetation area increased, the LAI was significantly underestimated (~60%) for the mixed pixels.

Moreover, it should be noted that MODIS LAI products are composited using daily LAI retrieval at 8-day interval, and daily LAI from the main algorithm has higher priority than the back-up algorithm when selecting the composited LAI value. However, given that the main algorithm has strict boundaries for both red and NIR bands (Fig. 7a), the pixel LAI could be generated from the back-up algorithm once BRFs exceed the boundaries of the main algorithm. In this case, the LAI retrieval from another day would be selected. Due to uncertainties in BRFs on different days, the impact of the specific day used to derive the composited LAI product before and after the correction of water effects should be necessarily taken into account in the practice of LAI retrievals.

Based on the above analysis, it is believed that water endmember in land-water mixed pixels can directly change LAI retrievals. Furthermore, the water endmember also plays a role in the selection of the composited date and thus affects the final value of LAI product. The number of pixels and the proportion of the same DOY to generate both RWE and MODIS 8-day LAI retrievals in different WAFs are displayed in Fig. 8. Specifically, the number of pixels decreased with increasing WAF (Fig. 8a), and the similar trend was also observed for the proportion of pixels from the same DOY (Fig. 8b). The result indicates that when WAF is large, the day that is selected for the 8-day LAI composition will be

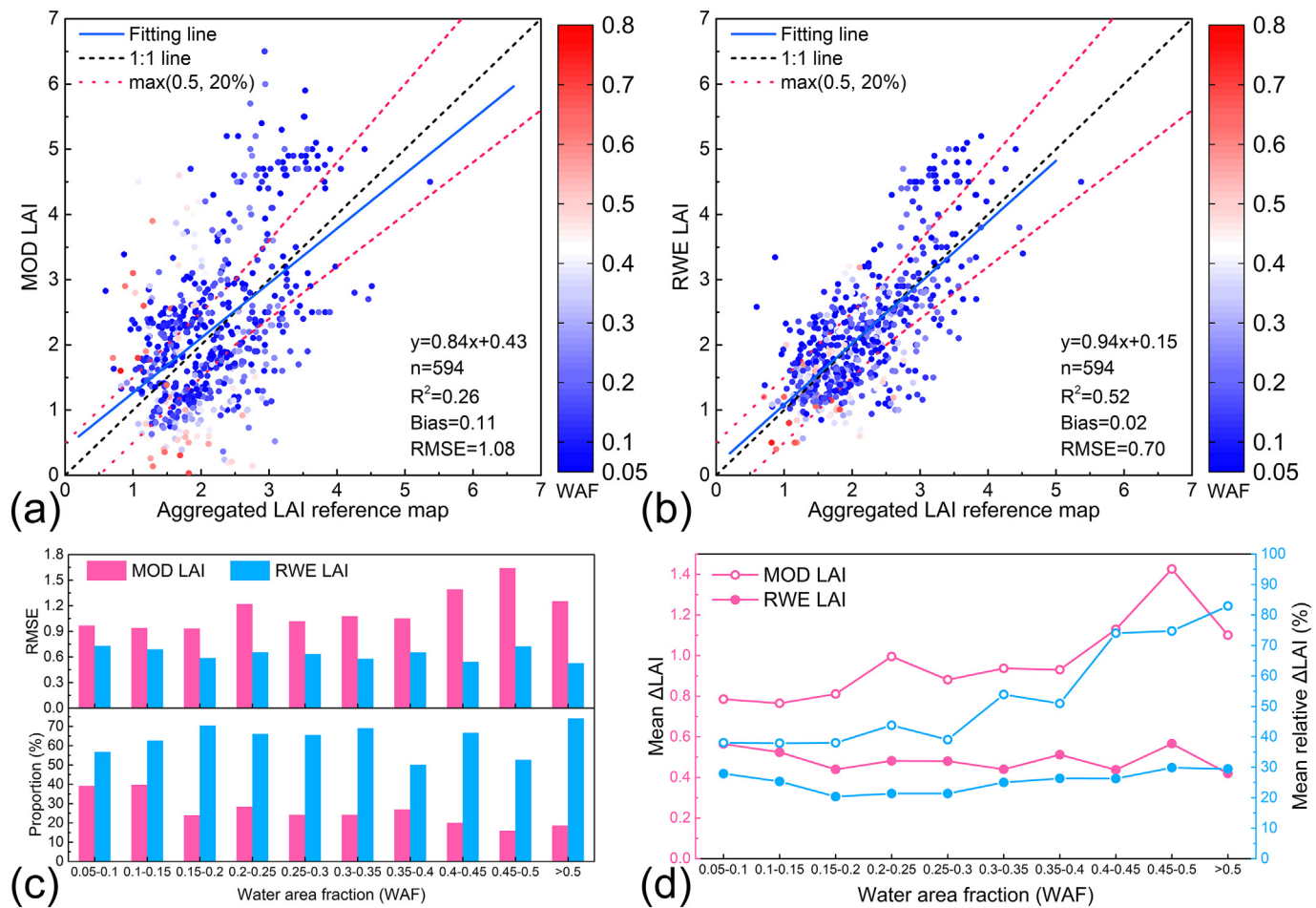


Fig. 6. The scatter plot for (a) the comparison between MODIS LAI and the aggregated 30-m LAI reference map and (b) the comparison between RWE LAI and the aggregated 30-m LAI reference map for three sites. The WAFs in different pixels are depicted by different colors. (c) shows the RMSE between RWE/MODIS LAI retrievals and aggregated LAI reference maps in different WAFs (upper panel), and the proportion of pixels satisfying the uncertainty requirement ($\text{max}(0.5, 20\%)$) from GCIN in different WAFs (lower panel). (d) displays the trends of mean ΔLAI (red line, $\Delta\text{LAI} = |\text{LAI}_{\text{retrievals}} - \text{LAI}_{\text{reference}}|$) and mean relative ΔLAI (blue line, relative $\Delta\text{LAI} = 100 \times |\text{LAI}_{\text{retrievals}} - \text{LAI}_{\text{reference}}| / \text{LAI}_{\text{reference}}$) in different WAFs. (For interpretation of the references to color in this figure legend, the reader is referred to the web version of this article.)

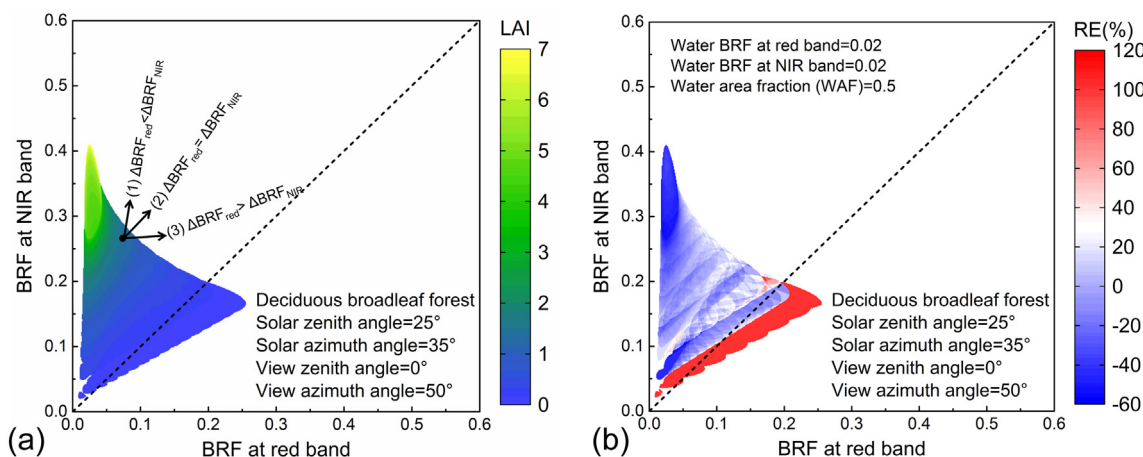


Fig. 7. (a) The change of simulated LAI with BRFs in the red and NIR bands from the main LAI retrieval algorithm. The main algorithm retrieves an LAI value only if the observed pair ($\text{BRF}_{\text{red}}, \text{BRF}_{\text{NIR}}$) of BRFs falls within the retrieval domain. This case was simulated for a deciduous broadleaf forest, with solar zenith angle of 25°, solar azimuth angle of 35°, view zenith angle of 0°, and view azimuth angle of 50°. (b) The LAI relative error ($\text{RE} = 100 \times (\text{LAI}_{\text{land-water mixed pixels}} - \text{LAI}_{\text{actual}}) / \text{LAI}_{\text{actual}}$) for the land-water mixed pixels changes with different BRFs in the red and NIR bands for the vegetation part. The water BRFs at red and NIR bands were both 0.02, while the WAF was 0.5. (For interpretation of the references to color in this figure legend, the reader is referred to the web version of this article.)

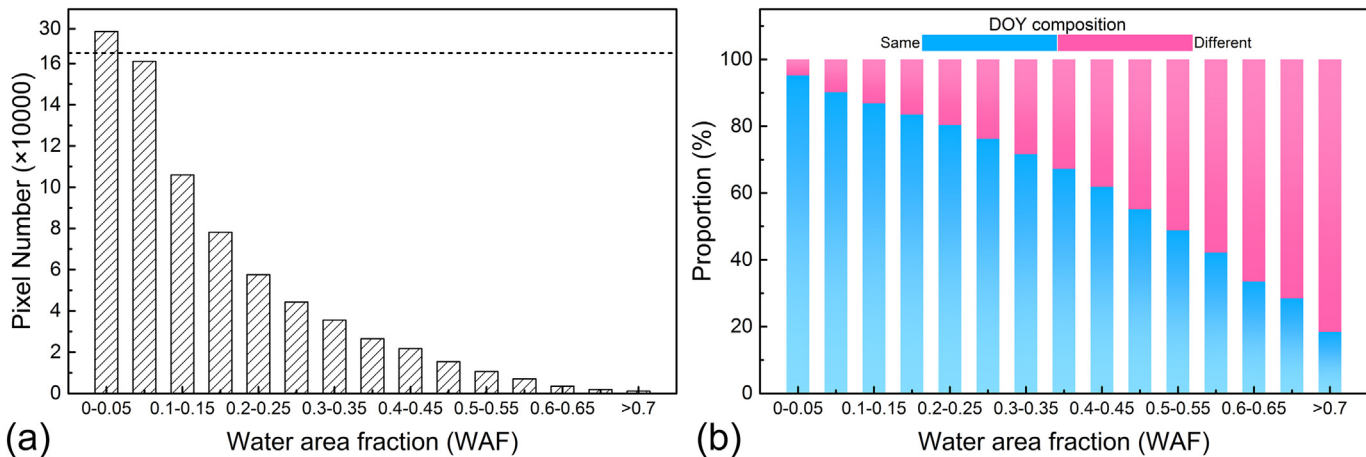


Fig. 8. The statistical results of (a) the number of pixels and (b) the proportions of the same DOY and different DOYs in different WAFs. The same DOY in (b) indicates that the specific day to generate the 8-day composited value for RWE LAI retrievals was identical to that for MODIS LAI products.

obviously changed. Therefore, the water effects for both the same DOY and different DOYs used to composite the 8-day MODIS and RWE LAI retrievals should be comprehensively analyzed.

4.4. Intercomparison with MODIS C6 LAI products

To further evaluate water effects on LAI retrievals for the land-water mixed pixel in practice, the RWE LAI were compared to MODIS LAI in two ways, i.e., using the same DOY (Fig. 9a) and different DOYs (Fig. 9b) to generate the 8-day LAI products, respectively. For the same DOY, the bias was < 0 for all different WAFs, indicating that LAI would be underestimated if a pixel was mixed with water. Moreover, the negative effect of water mixture would be larger if a pixel were occupied by more water (WAF increased). It is noteworthy that the water effect is

relevant to the LAI magnitude shown in Fig. 9a. When LAI was low (< 1) or the WAF was low (< 0.4), the MODIS LAI was slightly underestimated (< 0.4). However, as the increase of LAI or WAF, MODIS LAI showed an obvious underestimation that can reach -1.8 ($4 < \text{LAI} < 4.5$ and $0.35 < \text{WAF} < 0.4$).

In terms of different DOYs, the systematic error of MODIS LAI caused by water mixture was different at various LAI magnitudes (Fig. 9b). For the small LAI and WAF ($\text{LAI} < 2$ and $\text{WAF} < 0.2$), no systematic error was observed even though the composed DOY was changed. With the increase in LAI or WAF, MODIS LAI exhibited an obvious overestimation (approximately 1). However, when both LAI and WAF were large, MODIS LAI presented a significant underestimation (approximately -1.4). These results could be explained by the variations in BRFs and WAFs caused by land-water mixed pixels. For

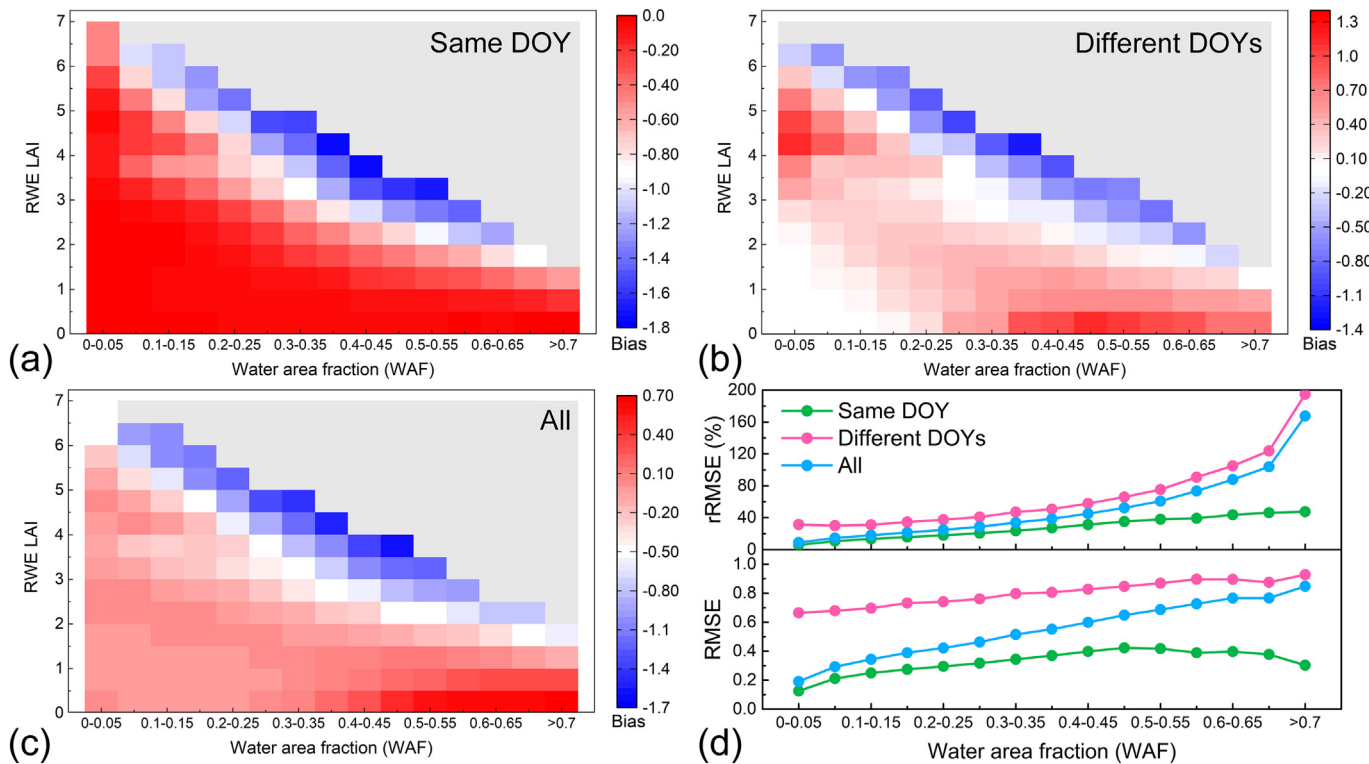


Fig. 9. The comparison between RWE and MODIS LAI retrievals in different WAFs and LAIs. (a), (b) and (c) are the differences in the LAI retrievals at the same, different and all DOYs used to generate the 8-day LAI products, respectively. The gray color indicates that no LAI retrievals were available. (d) indicates the variations in RMSE and relative RMSE (rRMSE) at different WAFs.

example, a large WAF always corresponds to a small land area and then results in large land BRFs within a mixed pixel (Eq. (3)). If the increase in LAI caused by the increase in land BRFs was greater than the decrease in LAI caused by decreasing land area, the underestimation of MODIS LAI would be observed. The results in Fig. 9b indicate that MODIS LAI was underestimated for large LAI and WAF, while it was comparable or overestimated in the comparison with RWE LAI for low LAI or WAF.

Additionally, we performed a comparative analysis using all MODIS and RWE LAI retrievals (Fig. 9c). At different LAI magnitudes, MODIS LAI showed significant overestimation, with the maximum almost reached 0.7 when the WAF was large but LAI was low, which was primarily observed for sparse needleleaf forest or savanna based on the MODIS land cover dataset. For the case in which both WAF and LAI were relatively large, MODIS LAI displayed considerable underestimation (-1.4). Furthermore, the RMSE and rRMSE that characterize the absolute difference between MODIS LAI and RWE LAI both increased as WAF increased, with the maximum of over 0.9 and 100%, respectively (Fig. 9d). Obviously, the influence of LAI retrievals using different DOYs was much larger than that using the same DOY. Therefore, due to different uncertainties of BRFs or varying vegetation status in different DOYs of the 8-day period, the influence of selecting different DOYs to generate LAI product for land-water mixed pixels cannot be ignored in the LAI retrieval algorithm.

4.5. Limitations and future prospects

First, the mixture of water and vegetation within a pixel can be divided into two types: (1) the background of the vegetation is soil, i.e., vegetation and water are in different locations; (2) the background of the vegetation is water, i.e., vegetation and water are in the same location, such as flooded or aquatic vegetation in wetlands. Only the first case was considered in this study. However, the water background also significantly affects the anisotropic reflectance of the vegetation canopy (Sun et al., 2017), which should be taken into account for LAI retrievals. Fortunately, canopy models have been developed for both flooded vegetation (Beget et al., 2013) and aquatic vegetation (Zhou et al., 2015), and the wetland can be well identified using different time-series vegetation indices (e.g. NDVI, normalized difference water index (NDWI), land surface water index (LSWI)) based on various classification schemes (e.g., decision tree or random forest) (Mahdavi et al., 2017). Therefore, the influence of the water background for LAI retrievals can be corrected in future work. Second, due to the limited spatial coverage of ground-based LAI reference maps for coarse-resolution land-water mixed pixels, the performance of the RWE method was primarily evaluated over the needleleaf forest in this study. Adding more ground measurements, especially from various biomes, may achieve a more robust evaluation result for the RWE method. Third, the land-water mixed pixel LAI retrievals are also influenced by the accuracy of the WAF extracted from 30-m land cover maps. Since the 30-m land cover maps are currently available only for the years 2000 and 2010, the variation in the water area in different observation years or even seasons may introduce undesired uncertainties to the LAI retrievals. Therefore, other datasets that can provide the water spatial distribution information in various years need to be considered. For instance, the water pixel has been identified in the long-term Landsat surface reflectance products (Claverie et al., 2015; Vermote et al., 2016) provided by the U.S. Geological Survey (USGS). The accuracy of LAI retrievals can be further improved through the RWE method as long as more accurate WAF information can be obtained.

In this study, the RWE was used in four MODIS tiles for which both land-water mixed pixels and high-resolution LAI reference maps were available to evaluate its performance on LAI retrievals. Further efforts are particularly necessary for the application of the RWE method at the global scale. Based on the global 30-m land cover maps, the result of global WAF (excluding ocean) in the 500-m pixel grid was calculated

(Fig. 10a). The land-water mixed pixels are located in almost all regions worldwide. The geographical distribution of land-water mixed pixels is strongly clustered in the northern hemisphere, especially in Canada, Russia, southeast China and the eastern US. Based on MODIS land cover product, the proportion of land-water mixed pixels for each biome was calculated, showing that the pixels mixed with water accounted for 13.9% of all mixed pixels (Fig. 10b). Among all biomes, the largest proportion of land-water mixed pixels occurred for shrubs (20.3%) followed by evergreen needleleaf forest (15.9%) and grasses/cereal crops (14.4%). Such high numbers of water-mixed pixels highlights the necessity of considering the water effects on LAI retrievals at the global scale. Additionally, as described in Section 2.2, the water endmember reflectance in mixed pixels is determined by that of adjacent pure water pixels. We calculated the proportion of water pixels for all valid MODIS tiles ($N = 476$) and found that almost all tiles have land-water mixed pixels together with pure water pixels (245 out of 250 tiles, Fig. 10c), among which 94.8% (237 out of 250 tiles) of land-water mixed tiles contains > 100 pure water pixels, indicating the potential of using the RWE method for the generation of global LAI product.

5. Conclusions

The water mixture in the moderate- or coarse-resolution pixel grid increases the uncertainty of LAI retrievals due to the negative impacts of water on the whole pixel reflectance. In this study, a novel RWE method was proposed to reduce the water effects for LAI retrievals over the land-water mixed pixels. The RWE first calculated the WAF in the 500-m pixel grid based on the 30-m land cover maps to identify pure water and land-water mixed pixels. Then, the water endmember reflectance in mixed pixels was generated using the adjacent pure water pixels associated with a spatio-temporal filter method. Finally, the extracted subpixel land reflectance was used to estimate the whole pixel LAI based on the WAF and the latest retrieval algorithm for the MODIS C6 LAI products. The evaluation results indicated the uncertainty of derived water endmember reflectance had minor effects on LAI retrievals. Confrontation with aggregated 30-m LAI reference maps in the 500-m pixel grid shows RWE LAI retrievals had higher accuracy than MODIS LAI products over land-water mixed pixels, especially for mixed pixels with larger WAFs. The mean relative difference between RWE LAI and aggregated 30-m LAI did not vary with WAF, indicating that water effects were significantly reduced. Furthermore, the water endmember in land-water mixed pixels not only changed the LAI values directly but also influenced the selection of the DOY used to composite the 8-day LAI products. Overall, a comprehensive analysis of these two aspects shows that the total error of LAI retrievals caused by water effects can reach 0.9. With the promising results presented in this study, RWE holds great potentials for the improvement of global LAI retrievals given the existence of a large proportion of land-water mixed pixels at the global scale. However, this method is specific to land-water mixed pixels. The effect of other land cover mixtures in the moderate- or coarse-resolution pixel grid on LAI retrievals and the associated processing method are needed to be considered in future work.

CRediT authorship contribution statement

Baodong Xu:Methodology, Software, Writing - original draft.
Jing Li:Conceptualization, Methodology, Writing - review & editing.
Taejin Park:Methodology, Software. **Qinhuo Liu:**Writing - review & editing, Supervision. **Yelu Zeng:**Software, Validation. **Gaofei Yin:**Investigation, Software. **Kai Yan:**Validation. **Chi Chen:**Investigation, Software. **Jing Zhao:**Formal analysis. **Weiliang Fan:**Software, Validation. **Yuri Knyazikhin:**Conceptualization. **Ranga B. Myneni:**Conceptualization, Supervision.

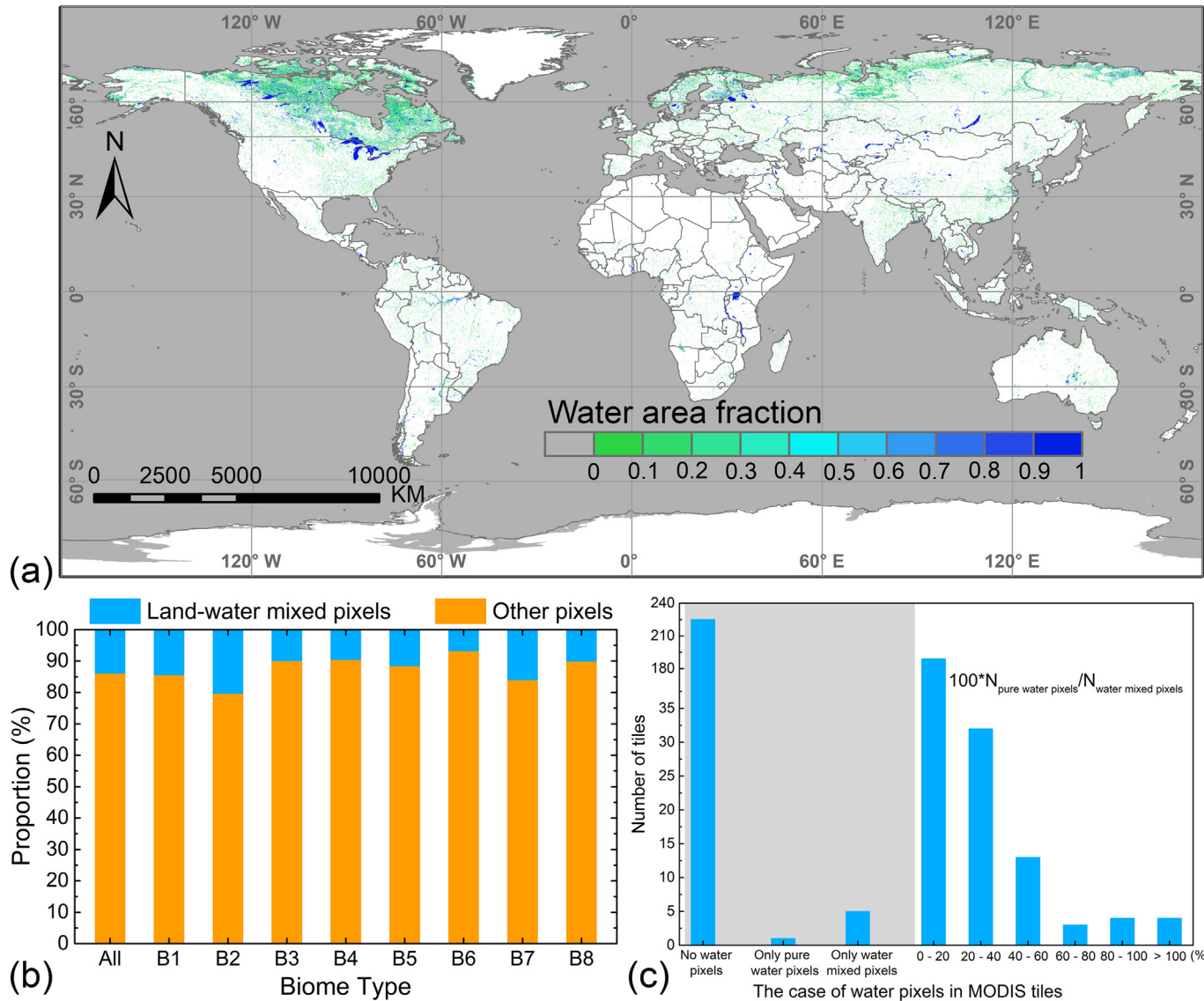


Fig. 10. (a) Global spatial distribution of WAF in a 500-m pixel grid. White areas refer to the land without water, and the gray background represents ocean areas. (b) The proportions of land-water mixed pixels in all mixed pixels for each biome. The definition of biome types were from the Land_Cover_Type3 classification provided by MODIS land cover products (MCDLCHKM). B1: Grasses/cereal crops; B2: Shrubs; B3: Broadleaf crops; B4: Savanna; B5: Evergreen Broadleaf Forest (EBF); B6: Deciduous Broadleaf Forest (DBF); B7: Evergreen Needleleaf Forest (ENF); B8: Deciduous Needleleaf Forest (DNF). (c) The number of MODIS tiles for 4 cases referring to water pixels in each tile, i.e., no water pixels, only pure water pixels, only water mixed pixels, and both pure water and water mixed pixels.

Declaration of competing interest

The authors declare that they have no known competing financial interests or personal relationships that could have appeared to influence the work reported in this paper.

Acknowledgements

This work was supported by the National Key Research and Development Program of China (2017YFA0603001), National Natural Science Foundation of China (41671374), the GF6 Project (30-Y20A03-

9003-17/18), and the Fundamental Research Funds for the Central Universities (2662018QD066). We thank Oak Ridge National Laboratory Distributed Active Archive Center (ORNL DAAC) for providing the 30-m LAI reference maps. The 30-m land cover datasets were provided by the National Geomatics Center of China. We are also grateful for the Landsat Surface Reflectance products courtesy of the U.S. Geological Survey Earth Resources Observation and Science Center for providing the Landsat TM/ETM+ surface reflectance data. We would like to thank the three anonymous reviewers for their constructive comments and suggestions that helped to improve the paper.

Appendix A. The process of the spatio-temporal filtered (mTSF) method for generating high-quality reflectance of pure water pixels

The critical process of the mTSF method is the Cressman analysis shown in Eq. (A1), which corrects the water reflectance of pixels in Levels 1–2 by using residuals between background reflectance and observed reflectance on 5 observation dates. Here the background reflectance is calculated as the average of high-quality pure water reflectance among all reflectances of pure water pixels on the specific date (t) in different years.

$$\rho(t_i) = \rho_b(t_i) + \frac{\sum_{j=i-2}^{i+2} w(t_i, t_j)[\rho_o(t_j) - \rho_b(t_j)]}{\sum_{j=i-2}^{i+2} w(t_i, t_j)}, \quad w(t_i, t_j) = \max\left(0, \frac{R^2 - d_{ij}^2}{R^2 + d_{ij}^2}\right) \quad (A1)$$

where t_i and t_j represent the DOY of pixel i and pixel j , respectively. ρ_o and ρ_b are the observation and background water reflectance on date t . R is a constant ($=24$) in this study and d is the DOY distance between t_i and t_j . Thus, the valid observation (ρ_o) and background (ρ_b) water reflectance are important to generate the high-quality reflectance for pixels of Levels 1–2. Specifically, the mTSF method includes three main steps as follows:

Step 1: Estimating the background water reflectance to filter the Levels 1–2 observations

The background reflectance of pure water pixels is of great importance because it provides the reference for filtering the observation reflectance of inferior quality. In this study, MOD09A1 products from 2000 to 2017 were used to calculate the background water reflectance based on 3 different cases as follows:

Case 1. For each pure water pixel, the 18 observations were from the same DOY during 2000–2017. If the number of Level 0 pixels in these 18 observations was > 6 , the pixel values were averaged to represent the background water reflectance. Otherwise, the background water reflectance could not be calculated because of the inadequate high-quality observations. Then these unprocessed pixels went into **Case 2**.

Case 2. For missing values on a certain DOY among 46 observations (8-day interval) from the averaged pixels in 2000–2017, the TIMSESAT SG (Savitzky-Golay) filter (Jönsson and Eklundh, 2002, 2004) was applied to generate the background water reflectance of these pixels based on the successfully calculated reflectance from **Case 1**. However, this step may also fail when there are too many missing values in the temporal profile. If the filter process was successful, the generated reflectance was used to replace the missing values in **Case 1**. Otherwise, the remaining pixels proceeded into **Case 3**.

Case 3. In this step, the pure water pixels with inferior quality inherited from **Case 2** were further processed using the Level 0 reflectance from **Case 1**. For a calculated pixel, the pure water reflectance was selected by increasing the window size ($3 \times 3, 5 \times 5\dots$) according to the distance from the pixel. Once at least 10 Level 0 pixels were found, the pixel value would be set to the average of all valid pixels. Based on **Cases 1–3**, the background reflectance for Levels 1–2 pure water pixels was derived.

Step 2: Temporal filtering for the reflectance of Level 2 observations on a certain DOY

Due to the invalid reflectances (> 0.1 or ≤ 0) for Level 2 pixels, it is necessary to fill the missing values using the temporal filtering method. First, a smoothing window size was set to 5, and then the invalid value was calculated using the SG method. If the reflectance was not available in the fitting window, the corresponding background value was used as an input. Finally, the reference observation was calculated for all Level 2 pixels, which would be used in step 3.

Step 3: Combining background and observed water reflectance using Cressman analysis to generate high-quality reflectance of pure water pixels

Based on the QA information and the valid range of water reflectances, Level 0 pure water pixels can be directly used as the reference reflectance to derive the water endmember reflectance in mixed pixels. Then, the Cressman analysis method in Eq. (A1) was applied to the processed Levels 1–2 pixels based on steps 1–2. Finally, the continuous high-quality reflectance was generated for all pure water pixels.

Appendix B. Supplementary data

Supplementary data to this article can be found online at <https://doi.org/10.1016/j.rse.2020.111700>.

References

- Baret, F., Hagolle, O., Geiger, B., Bicheron, P., Miras, B., Huc, M., Berthelot, B., Niño, F., Weiss, M., Samain, O., Roujeau, J.L., Leroy, M., 2007. LAI, FAPAR and fCover CYCLOPES global products derived from VEGETATION: part 1: principles of the algorithm. *Remote Sens. Environ.* 110, 275–286.
- Baret, F., Weiss, M., Lacaze, R., Camacho, F., Makhmara, H., Pacholczyk, P., Smets, B., 2013. GEOV1: LAI and FAPAR essential climate variables and FCOVER global time series capitalizing over existing products. Part1: principles of development and production. *Remote Sens. Environ.* 137, 299–309.
- Beget, M.E., Bettachini, V.A., Di Bella, C.M., Baret, F., 2013. SAILHFlood: a radiative transfer model for flooded vegetation. *Ecol. Model.* 257, 25–35.
- Bi, J., Knyazikhin, Y., Choi, S., Park, T., Barichivich, J., Ciais, P., Fu, R., Ganguly, S., Hall, F., Hilker, T., Huete, A., Jones, M., Kimball, J., Lyapustin, A.I., Möttus, M., Nemani, R.R., Piao, S., Poulter, B., Saleska, S.R., Saatchi, S.S., Xu, L., Zhou, L., Myneni, R.B., 2015. Sunlight mediated seasonality in canopy structure and photosynthetic activity of Amazonian rainforests. *Environ. Res. Lett.* 10, 064014.
- Bonan, G.B., 1995. Land-atmosphere interactions for climate system models: coupling biophysical, biogeochemical, and ecosystem dynamical processes. *Remote Sens. Environ.* 51, 57–73.
- Bratic, G., Brovelli, M.A., Molinari, M.E., 2018. A free and open source tool to assess the accuracy of land cover maps: implementation and application to Lombardy region (Italy). *Int. Arch. Photogramm. Remote Sens. Spatial Inf. Sci.* XLII-3, 87–92.
- Brovelli, A.M., Molinari, E.M., Hussein, E., Chen, J., Li, R., 2015. The first comprehensive accuracy assessment of GlobeLand30 at a national level: methodology and results. *Remote Sens.* 7, 4191–4212.
- Camacho, F., Cernicharo, J., Lacaze, R., Baret, F., Weiss, M., 2013. GEOV1: LAI, FAPAR essential climate variables and FCOVER global time series capitalizing over existing products. Part 2: validation and intercomparison with reference products. *Remote Sens. Environ.* 137, 310–329.
- Chen, J.M., 1999. Spatial scaling of a remotely sensed surface parameter by contexture. *Remote Sens. Environ.* 69, 30–42.
- Chen, J.M., Black, T.A., 1992. Defining leaf area index for non-flat leaves. *Plant Cell Environ.* 15, 421–429.
- Chen, J.M., Pavlic, G., Brown, L., Cihlar, J., Leblanc, S.G., White, H.P., Hall, R.J., Peddle, D.R., King, D.J., Trofymow, J.A., Swift, E., Van der Sanden, J., Pellikka, P.K.E., 2002. Derivation and validation of Canada-wide coarse-resolution leaf area index maps using high-resolution satellite imagery and ground measurements. *Remote Sens. Environ.* 80, 165–184.
- Chen, J., Ban, Y., Li, S., 2014. China: open access to earth land-cover map. *Nature* 514, 434.
- Chen, J., Chen, J., Liao, A., Cao, X., Chen, L., Chen, X., He, C., Han, G., Peng, S., Lu, M., Zhang, W., Tong, X., Mills, J., 2015. Global land cover mapping at 30 m resolution: a POK-based operational approach. *ISPRS J. Photogramm. Remote Sens.* 103, 7–27.
- Claverie, M., Vermote, E.F., Franch, B., Masek, J.G., 2015. Evaluation of the Landsat-5 TM and Landsat-7 ETM+ surface reflectance products. *Remote Sens. Environ.* 169, 390–403.
- Fang, H., Wei, S., Liang, S., 2012. Validation of MODIS and CYCLOPES LAI products using global field measurement data. *Remote Sens. Environ.* 119, 43–54.
- Fang, H., Li, W., Myneni, R.B., 2013. The impact of potential land cover misclassification on MODIS leaf area index (LAI) estimation: a statistical perspective. *Remote Sens.* 5, 830–844.
- Fernandes, R.A., Abduelgasim, A., Sylvain, L., Khurshid, S.K., Butson, C., 2005. Leaf Area Index Maps at 30-M Resolution, Selected Sites, Canada. ORNL DAAC, Oak Ridge, Tennessee, USA.
- Ganguly, S., Schull, M.A., Samanta, A., Shabanov, N.V., Milesi, C., Nemani, R.R., Knyazikhin, Y., Myneni, R.B., 2008. Generating vegetation leaf area index earth system data record from multiple sensors. Part 1: theory. *Remote Sens. Environ.* 112, 4333–4343.
- Garrigues, S., Allard, D., Baret, F., Weiss, M., 2006. Influence of landscape spatial heterogeneity on the non-linear estimation of leaf area index from moderate spatial resolution remote sensing data. *Remote Sens. Environ.* 105, 286–298.
- Garrigues, S., Lacaze, R., Baret, F., Morisette, J.T., Weiss, M., Nickeson, J.E., Fernandes,

- R., Plummer, S., Shabanov, N.V., Myneni, R.B., Knyazikhin, Y., Yang, W., 2008. Validation and intercomparison of global Leaf Area Index products derived from remote sensing data. *J. Geophys. Res.* 113, G02028.
- GCOS, 2011. Systematic Observation Requirements for Satellite-Based Products for Climate, 2011 Update, Supplemental Details to the Satellite-Based Component of the Implementation Plan for the Global Observing System for Climate in Support of the UNFCCC (2010 Update), Reference Number GCOS-154. pp. 138.
- Jin, Z., Tian, Q., Chen, J.M., Chen, M., 2007. Spatial scaling between leaf area index maps of different resolutions. *J. Environ. Manag.* 85, 628–637.
- Jonckheere, I., Fleck, S., Nackaerts, K., Muys, B., Coppin, P., Weiss, M., Baret, F., 2004. Review of methods for in situ leaf area index determination: part I. Theories, sensors and hemispherical photography. *Agric. For. Meteorol.* 121, 19–35.
- Jönsson, P., Eklundh, L., 2002. Seasonality extraction by function fitting to time-series of satellite sensor data. *IEEE Trans. Geosci. Remote Sens.* 40, 1824–1832.
- Jönsson, P., Eklundh, L., 2004. TIMESAT—a program for analyzing time-series of satellite sensor data. *Comput. Geosci.* 30, 833–845.
- Knyazikhin, Y., Martonchik, J.V., Myneni, R.B., Diner, D.J., Running, S.W., 1998. Synergistic algorithm for estimating vegetation canopy leaf area index and fraction of absorbed photosynthetically active radiation from MODIS and MISR data. *J. Geophys. Res. Atmos.* 103, 32257–32275.
- Liang, S.L., Fang, H.L., Chen, M.Z., Shuey, C.J., Walther, C., Daughtry, C., Morissette, J., Schaaf, C., Strahler, A., 2002. Validating MODIS land surface reflectance and albedo products: methods and preliminary results. *Remote Sens. Environ.* 83, 149–162.
- Liu, J., Chen, J.M., Cihlar, J., Park, W.M., 1997. A process-based boreal ecosystem productivity simulator using remote sensing inputs. *Remote Sens. Environ.* 62, 158–175.
- Mahdavi, S., Salehi, B., Granger, J., Amani, M., Brisco, B., Huang, W., 2017. Remote sensing for wetland classification: a comprehensive review. *GISci. Remote Sens.* 55, 623–658.
- Manakos, I., Chatzopoulos-Vouzoglani, K., Petrou, I.Z., Filchev, L., Apostolakis, A., 2015. Globalland30 mapping capacity of land surface water in Thessaly, Greece. *Land* 4, 1–18.
- Masek, J.G., Vermote, E.F., Saleous, N.E., Wolfe, R., Hall, F.G., Huemmrich, K.F., Feng, G., Kutler, J., Teng-Kui, L., 2006. A Landsat surface reflectance dataset for North America, 1990–2000. *IEEE Geosci. Remote Sens. Lett.* 3, 68–72.
- Morissette, J.T., Baret, F., Privette, J.L., Myneni, R.B., Niceson, J.E., Garrigues, S., Shabanov, N.V., Weiss, M., Fernandes, R.A., Leblanc, S.G., Kalacska, M., Sanchez-Azofeifa, G.A., Chubey, M., Rivard, B., Stenberg, P., Rautiainen, M., Voipio, P., Manninen, T., Pilant, A.N., Lewis, T.E., Iijames, J.S., Colombo, R., Meroni, M., Busetto, L., Cohen, W.B., Turner, D.P., Warner, E.D., Petersen, G.W., Seufert, G., Cook, R., 2006. Validation of global moderate-resolution LAI products: a framework proposed within the CEOS land product validation subgroup. *IEEE Trans. Geosci. Remote Sens.* 44, 1804–1817.
- Myneni, R.B., Hoffman, S., Knyazikhin, Y., Privette, J.L., Glassy, J., Tian, Y., Wang, Y., Song, X., Zhang, Y., Smith, G.R., Lotsch, A., Friedl, M., Morissette, J.T., Votava, P., Nemani, R.R., Running, S.W., 2002. Global products of vegetation leaf area and fraction absorbed PAR from year one of MODIS data. *Remote Sens. Environ.* 83, 214–231.
- Sellers, P.J., Dickinson, R.E., Randall, D.A., Betts, A.K., Hall, F.G., Berry, J.A., Collatz, G.J., Denning, A.S., Mooney, H.A., Nobre, C.A., Sato, N., Field, C.B., Henderson-Sellers, A., 1997. Modeling the exchanges of energy, water, and carbon between continents and the atmosphere. *Science* 275, 502–509.
- Shabanov, N.V., Huang, D., Yang, W.Z., Tan, B., Knyazikhin, Y., Myneni, R.B., Ahl, D.E., Gower, S.T., Huete, A.R., Aragao, L.E.O.C., Shimabukuro, Y.E., 2005. Analysis and optimization of the MODIS leaf area index algorithm retrievals over broadleaf forests. *IEEE Trans. Geosci. Remote Sens.* 43, 1855–1865.
- Simonich, S.L., Hites, R.A., 1994. Importance of vegetation in removing polycyclic aromatic hydrocarbons from the atmosphere. *Nature* 370, 49.
- Sun, F., Sun, W., Chen, J., Gong, P., 2012. Comparison and improvement of methods for identifying waterbodies in remotely sensed imagery. *Int. J. Remote Sens.* 33, 6854–6875.
- Sun, T., Fang, H., Liu, W., Ye, Y., 2017. Impact of water background on canopy reflectance anisotropy of a paddy rice field from multi-angle measurements. *Agric. For. Meteorol.* 233, 143–152.
- Tian, Y., Zhang, Y., Knyazikhin, Y., Myneni, R.B., Glassy, J.M., Dedieu, G., Running, S.W., 2000. Prototyping of MODIS LAI and FPAR algorithm with LASUR and LANDSAT data. *IEEE Trans. Geosci. Remote Sens.* 38, 2387–2401.
- Tian, Y., Wang, Y., Zhang, Y., Knyazikhin, Y., Bogaert, J., Myneni, R.B., 2002. Radiative transfer based scaling of LAI retrievals from reflectance data of different resolutions. *Remote Sens. Environ.* 84, 143–159.
- Vermote, E.F., Kotchenova, S.Y., Ray, J.P., 2015. MODIS Surface Reflectance User's Guide (Version 1.4). MODIS L. Surf. Reflectance Sci. Comput. Facil. https://lpdaac.usgs.gov/documents/306/MOD09_User_Guide_V6.pdf.
- Vermote, E.F., Justice, C., Claverie, M., Franch, B., 2016. Preliminary analysis of the performance of the Landsat 8/OLI land surface reflectance product. *Remote Sens. Environ.* 185, 46–56.
- Wang, Y.J., Tian, Y.H., Zhang, Y., El-Saleous, N., Knyazikhin, Y., Vermote, E., Myneni, R.B., 2001. Investigation of product accuracy as a function of input and model uncertainties: case study with SeaWiFS and MODIS LAI/FPAR algorithm. *Remote Sens. Environ.* 78, 299–313.
- Weiss, M., Baret, F., Garrigues, S., Lacaze, R., 2007. LAI and FPAR CYCLOPES global products derived from VEGETATION. Part 2: validation and comparison with MODIS collection 4 products. *Remote Sens. Environ.* 110, 317–331.
- Wu, H., Tang, B., Li, Z., 2013. Impact of nonlinearity and discontinuity on the spatial scaling effects of the leaf area index retrieved from remotely sensed data. *Int. J. Remote Sens.* 34, 3503–3519.
- Xiao, Y., Zhao, W., Zhou, D., Gong, H., 2014a. Sensitivity analysis of vegetation reflectance to biochemical and biophysical variables at leaf, canopy, and regional scales. *IEEE Trans. Geosci. Remote Sens.* 52, 4014–4024.
- Xiao, Z., Liang, S., Wang, J., Chen, P., Yin, X., Zhang, L., Song, J., 2014b. Use of general regression neural networks for generating the GLASS leaf area index product from time-series MODIS surface reflectance. *IEEE Trans. Geosci. Remote Sens.* 52, 209–223.
- Xiao, Z., Liang, S., Wang, J., Xiang, Y., Zhao, X., Song, J., 2016. Long-time-series global land surface satellite leaf area index product derived from MODIS and AVHRR surface reflectance. *IEEE Trans. Geosci. Remote Sens.* 54, 5301–5318.
- Xiao, Z., Liang, S., Jiang, B., 2017. Evaluation of four long time-series global leaf area index products. *Agric. For. Meteorol.* 246, 218–230.
- Xu, S., Chen, J.M., Fernandes, R., Cihlar, J., 2004. Effects of subpixel water area fraction on mapping leaf area index and modeling net primary productivity in Canada. *Can. J. Remote. Sens.* 30, 797–804.
- Xu, B., Park, T., Yan, K., Chen, C., Zeng, Y., Song, W., Yin, G., Li, J., Liu, Q., Knyazikhin, Y., Myneni, R.B., 2018. Analysis of global LAI/FPAR products from VIIRS and MODIS sensors for spatio-temporal consistency and uncertainty from 2012–2016. *Forests* 9, 73–93.
- Yan, K., Park, T., Chen, C., Xu, B., Song, W., Yang, B., Zeng, Y., Liu, Z., Yan, G., Knyazikhin, Y., Myneni, R.B., 2018. Generating global products of LAI and FPAR from SNPP-VIIRS data: theoretical background and implementation. *IEEE Trans. Geosci. Remote Sens.* 56, 2119–2137.
- Yang, W., Tan, B., Huang, D., Rautiainen, M., Shabanov, N.V., Wang, Y.J., Privette, J.L., Huemmrich, K.F., Fensholt, R., Sandholt, I., Weiss, M., Ahl, D.E., Gower, S.T., Nemani, R.R., Knyazikhin, Y., Myneni, R.B., 2006. MODIS leaf area index products: from validation to algorithm improvement. *IEEE Trans. Geosci. Remote Sens.* 44, 1885–1898.
- Yin, G., Li, J., Liu, Q., Li, L., Zeng, Y., Xu, B., Yang, L., Zhao, J., 2015. Improving leaf area index retrieval over heterogeneous surface by integrating textural and contextual information: a case study in the Heihe river basin. *IEEE Geosci. Remote Sens. Lett.* 12, 359–363.
- Yin, G., Li, A., Jin, H., Zhao, W., Bian, J., Qu, Y., Zeng, Y., Xu, B., 2017. Derivation of temporally continuous LAI reference maps through combining the LAINet observation system with CACAO. *Agric. For. Meteorol.* 233, 209–221.
- Yu, W., Li, J., Liu, Q., Zeng, Y., Zhao, J., Xu, B., Yin, G., 2018. Global land cover heterogeneity characteristics at moderate resolution for mixed pixel modeling and inversion. *Remote Sens.* 10, 856–862.
- Yuan, H., Dai, Y., Xiao, Z., Ji, D., Shangguan, W., 2011. Reprocessing the MODIS Leaf Area Index products for land surface and climate modelling. *Remote Sens. Environ.* 115, 1171–1187.
- Zhou, G., Niu, C., Xu, W., Yang, W., Wang, J., Zhao, H., 2015. Canopy modeling of aquatic vegetation: a radiative transfer approach. *Remote Sens. Environ.* 163, 186–205.
- Zhu, Z., Piao, S., Myneni, R.B., Huang, M., Zeng, Z., Canadell, J.G., Ciais, P., Sitch, S., Friedlingstein, P., Arneth, A., Cao, C., Cheng, L., Kato, E., Koven, C., Li, Y., Lian, X., Liu, Y., Liu, R., Mao, J., Pan, Y., Peng, S., Penuelas, J., Poultier, B., Pugh, T.A.M., Stocker, B.D., Viovy, N., Wang, X., Wang, Y., Xiao, Z., Yang, H., Zaehle, S., Zeng, N., 2016. Greening of the earth and its drivers. *Nat. Clim. Chang.* 6, 791–795.